

Article

Mouse-Derived Isograft (MDI) In Vivo Tumor Models II. Carcinogen-Induced cMDI Models: Characterization and Cancer Therapeutic Approaches

Janette Beshay ^{1,†,‡}, Peter Jantscheff ^{1,*‡}, Thomas Lemarchand ², Cynthia Obodozie ¹, Christoph Schächtele ¹ and Holger Weber ^{1,*}

¹ In Vivo Pharmacology, ProQinase GmbH, Breisacher Str. 117, 79106 Freiburg, Germany; Janette_Beshay@web.de (J.B.); c.obodozie@proqinase.com (C.O.); c.schaechtele@proqinase.com (C.S.)

² TPL Pathology Labs, Sasbacher Str. 10, 79111 Freiburg, Germany; lemarchand@tpl-path-labs.com

* Correspondence: peter.jantscheff@t-online.de (P.J.); h.weber@proqinase.com (H.W.); Tel.: +49-7666-913-0396 (P.J.); +49-761-769996-1733 (H.W.)

† Current address: Charles River Discovery Research Services Germany GmbH, Am Flughafen 12-14, 79108 Freiburg, Germany.

‡ These authors contributed equally to this work.

Received: 1 December 2018; Accepted: 13 February 2019; Published: 19 February 2019



Abstract: In this second study, we established syngeneic in vivo models named carcinogen-induced mouse-derived isografts (cMDIs). Carcinogen-induced tumors were obtained during short-term observation (3–9 months) of CBA/J mice treated with various administration routes with 3-methylcholanthrene (MCA) or *N*-methyl-*N*-nitrosourea (MNU) as carcinogens. During necropsy, primary tumors and suspicious tissues were assessed macroscopically and re-transplanted (in PDX-like manner) into sex-matched syngeneic animals. Outgrowing tumors were histologically characterized as either spinocellular carcinoma (1/8) or various differentiated sarcomas (7/8). Growth curves of four sarcomas showed striking heterogeneity. These cMDIs were further characterized by flow cytometry, RNA sequencing, or efficacy studies. A variable invasion of immune cells into the tumors, as well as varying expression of tyrosine kinase receptor, IFN- γ signature, or immune cell population marker genes could be observed. Immune checkpoint inhibitor treatment (anti-mPD-1, anti-mCTLA-4, or a combination thereof) showed different responses in the various cMDI models. In general, cMDI models are carcinogen-induced tumors of low passage number that were propagated as tissue pieces in mice without any tissue culturing. Therefore, the tumors contained conserved tumor characteristics and intratumoral immune cell populations. In contrast to the previously described spontaneous MDI, carcinogen induction resulted in a greater number of individual but histologically related tumors, which were preferentially sarcomas.

Keywords: mouse tumor models; experimental cancer; mouse-derived isografts (MDIs); carcinogen-induced tumors; therapy; immune checkpoint inhibitors; immunocompetent animals; syngeneic

1. Introduction

In the accompanying paper, the establishment and characterization of a new type of experimental in vivo cancer model, so-called mouse-derived isografts (MDIs) from spontaneous tumors (sMDIs), have been reported for the first time [1]. In the first part of this study, we introduced the establishment of nine histopathologically different sMDI tumor models in various mouse strains of both sexes, i.e., on different H-2 MHC class I haplotype backgrounds. The various sMDIs displayed heterogeneous take rates and growth curves. Preliminary efficacy data of immune checkpoint inhibitor (ICPI) treatment with anti-mPD-1, anti-mCTLA-4 antibodies, or a combination thereof, as well as treatment

with the chemotherapeutic gemcitabine, indicated different sensitivities to the different types of treatment. Additionally, flow cytometric analysis revealed variable tumor infiltration by immune cells compared to commonly used murine, cell line-based syngeneic standard tumor models [2]. RNA sequencing analysis showed different genetic modifications in the expression of tyrosine kinase receptors, IFN- γ -signature, or immune cell population markers comparing various MDI models [1]. The new models increased the quantity and quality of available syngeneic in vivo tumor models, since we generated novel primary adenocarcinomas, lymphomas, and histiocytic sarcoma/histiocyte-associated lymphomas. These new spontaneous tumor models enable studying the causes and molecular mechanisms of tumor development, as well as new therapeutic approaches, especially regarding the interaction between the immune system and the tumors.

In this second study, we established and characterized MDI cancer models by the induction of tumor formation by treatment with carcinogens 3-methylcholanthrene (MCA) or *N*-methyl-*N*-nitrosourea (MNU). The generated models were named carcinogen-induced MDI (cMDI) tumors. The goal of this study was to create more histopathologically closely related tumor entities derived from one mouse strain. Similar to sMDI tumors, cMDI tumors display low passage numbers and were propagated only in vivo as tissue pieces in syngeneic mice without any tissue culturing (in a patient-derived-xenograft (PDX)-like manner) resulting in rather conserved original tumor characteristics and immune cell populations [1]. Carcinogen induction resulted in sarcomas, in most cases, in H-2^k CBA/J mice of both sexes.

The approach of chemical induction of syngeneic mouse tumors by carcinogens has the advantage of inducing tumors faster and in larger numbers than it would take to wait for spontaneous tumors. However, some disadvantages are strain-specific differences in carcinogen sensitivity [3] and that the tumors are mostly sarcomas, which is a rarer tumor entity than adenocarcinomas, carcinomas, or lymphomas in patients and experimental animals [4]. Another difference to spontaneous tumors is a higher immunogenicity of carcinogen-induced tumor cells often caused by the expression of tumor-associated transplantation antigens (TATA) [5–7]. However, as demonstrated in rat MCA-induced fibrosarcomas, not all tumors (but about 75%) actually display such antigens [8].

In this study, we outline the establishment and characterization of tumors that are the result of carcinogen administration in H-2^k CBA/J mice of both sexes, and assess their use for future research.

2. Results

2.1. cMDI—Establishment History

For the establishment of cMDI, 12 female and 16 (originally, but eventually 13, since 3 animals died within 1–2 days after i.p. injection) male CBA/J mice were treated with MCA or MNU (Table 1).

Table 1. Carcinogen application schedules for the induction of carcinogen-induced mouse-derived isograft (cMDI) models.

	MNU		MCA	
	♀CBA/J Mice			
Application Route	s.c./imfp		s.c./i.m.	p.o.
Animal Number	4		4	4
	♂CBA/J Mice			
Application Route	s.c./i.v.	i.p.	s.c./i.m.	p.o.
Animal Number	4	1 (3) *	4	4

CBA/J mice of both sexes were treated with either 3-methylcholanthrene (MCA) or *N*-methyl-*N*-nitrosourea (MNU) via different application routes (s.c. subcutaneous, imfp intramammary fat pad, i.m. intramuscular, p.o. per oral, i.v. intravenous, i.p. intraperitoneally). * (3/4) animals died within 1–2 days after injection for unknown reasons.

Due to ethical reasons, i.e., critical weight loss, bad general condition, or externally detectable tumor growth, a necropsy of the animal was performed (Figure 1). The first necropsy was about two months after subcutaneous injection of MCA in a male CBA/J mouse (JA-2044) after developing a palpable subcutaneous tumor, and outgrowth of directly re-transplanted or frozen tumor pieces varied between 39 and 113 days after re-transplantation (Figure 2, Table 2). After about three months, a subcutaneous tumor was detected in another male mouse (JA-2041) treated subcutaneously with MCA. Also, during necropsy, suspicious prostate tissue was found and re-transplanted into syngeneic mice. Since only re-transplanted fresh or frozen subcutaneous tumor tissue led to stable outgrowth between 27 and 52 days (Figure 2, Table 2), collected frozen prostate tissue was not further pursued.

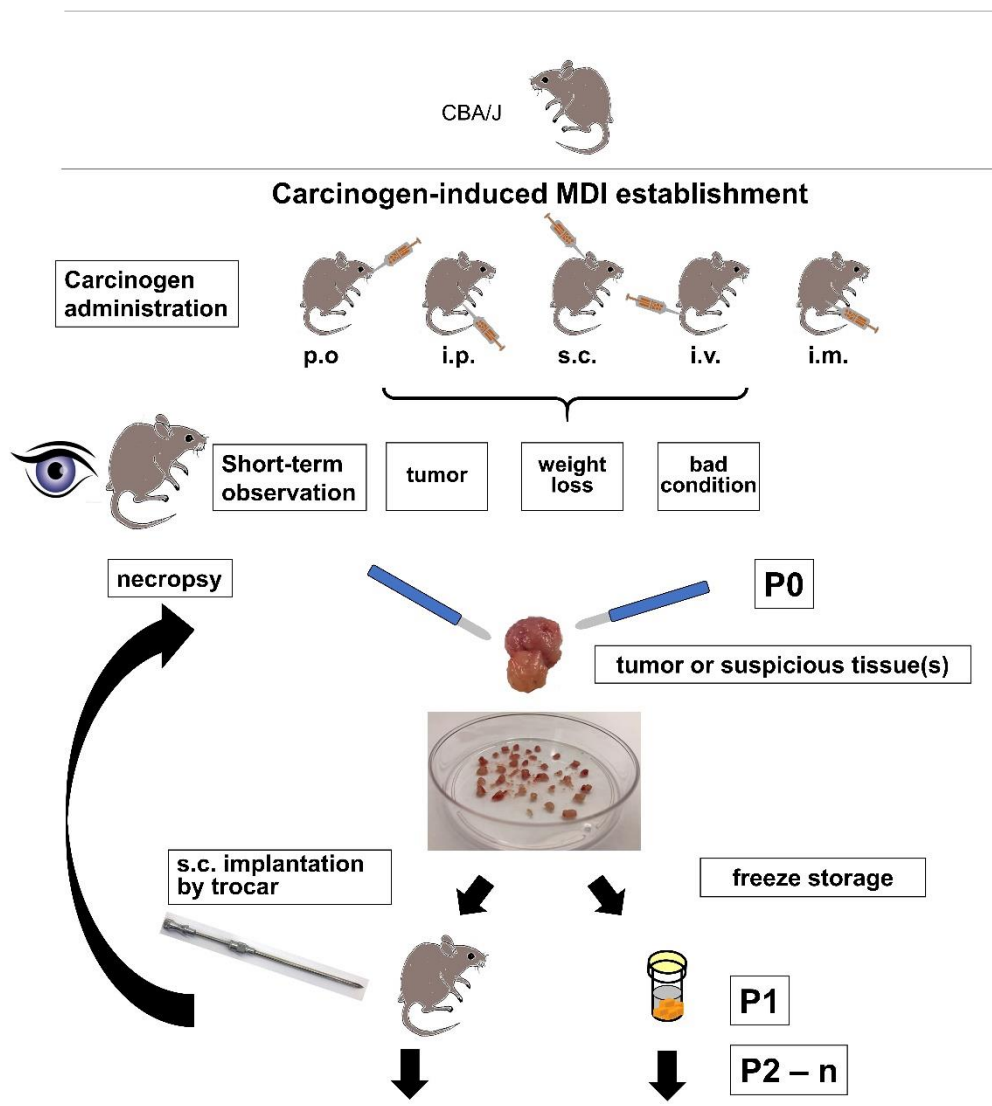


Figure 1. Scheme of cMDI establishment. Various carcinogen administration routes, as well as termination criteria, and general handling of tumor or other suspicious tissue samples are schematically summarized (P: passage numbers; P0: primary necropsy; P1: first passage of primary tumor; P2–n: second and further follow up passages).


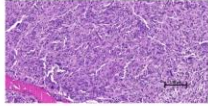


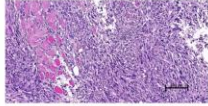


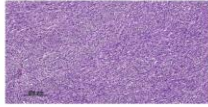


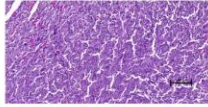
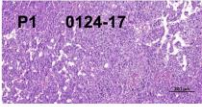

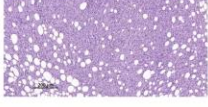


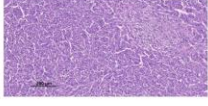

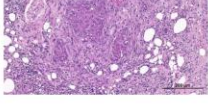
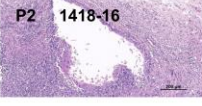




Mouse strain - sex	Tumor name	Diagnosis	Location of appearance in situ	HE staining of primary isolate	HE staining of re-transplanted tumor(s)
CBA/J ♀	JA-2011	Sarcoma (NOS) <i>anaplastic, with atypical mononuclear and multinucleate giant cells</i>			
CBA/J ♀	JA-2019	Sarcoma (NOS) <i>no giant cells, invades skeletal muscles and adipose tissue</i>			
CBA/J ♂	JA-2041	Sarcoma (NOS) <i>well differentiated to moderately anaplastic</i>			
CBA/J ♂	JA-2042	Sarcoma (NOS) <i>no giant cells, likely origin is integument of leg</i>			
CBA/J ♂	JA-2034	Sarcoma (NOS) <i>anaplastic, neoplastic cells exhibit moderate pleomorphism</i>			
CBA/J ♂	JA-2043	Sarcoma (NOS) <i>well differentiated to moderately anaplastic; no giant cells</i>			
CBA/J ♂	JA-2044	spinocellular Carcinoma <i>neoplastic proliferation from the skin</i>	no in situ foto		
SCID/bg (CBA/J) ♀	JA-2017	Sarcoma (NOS) <i>no giant cells, invades skeletal muscles and adipose tissue</i> - primary tumor CBA/J	 		

Figure 2. Histopathological characterization of established cMDI tumors. In situ location of primary tumor or suspicious tissue during necropsy, as well as hematoxylin and eosin (HE)-staining of resected primary and re-transplanted tumors using directly isolated (of passages P1–P4) or frozen tumor pieces (of passages P2F–P4F) are documented for eight cMDI models. NOS—sarcomas could not be otherwise specified by HE-staining. JA-2017 originated from female CBA/J but only grew in immune-deficient SCID/bg.

Table 2. Summary of established cMDI models.

Carcinogen-Induced MDI								
Tumor Name	JA-2044	JA-2011	JA-2019	JA-2034	JA-2041	JA-2042	JA-2043	JA-2017
Hematopoietic	no	no	no	no	no	no	no	no
Histopathological Diagnosis	spinocellular carcinoma	Sarcoma NOS, anaplastic,	Sarcoma NOS well-differentiated	Sarcoma NOS, anaplastic	Sarcoma NOS well-differentiated to moderately anaplastic	Sarcoma NOS well-differentiated to moderately anaplastic	Sarcoma NOS well-differentiated to moderately anaplastic	Sarcoma NOS, anaplastic,
Mouse Strain	CBA/J	CBA/J	CBA/J	CBA/J	CBA/J	CBA/J	CBA/J	CBA/J only in SCID/bg
Sex	♂	♀	♀	♂	♂	♂	♂	♀
Carcinogen (Appl. Route)	MCA (s.c.)	MNU (s.c.)	MCA (s.c.)	MNU (s.c.)	MCA (s.c.)	MCA (i.m.)	MCA (s.c.)	MCA (s.c.)
Estimated Growth Time (in Days)	39–113	14–35	16–63	29–55	25–105	25–46	17–36	14–28
Included Animals	frozen/directly (2/6) *	growth curve (12) **	growth curve (12)	frozen/directly (2/5)	growth curve (12)	growth curve (12)	frozen/directly (4/5)	frozen/directly (2/3) only in SCID/bg
Take Rate in % Number of Animals	63% 5/8	100% 12/12	100% 12/12	57% 4/7	83% 10/12	100% 12/12	100% 9/9	100% 5/5
Appearance (AP) on Days	nd	10–12	4–7	nd	7–11	9–13	nd	nd
Real Running Time (RRT) on Days (% Alive Animals)	nd	22 (87%) 30 (54%)	21 (75%) 25 (54%)	nd	25 (95%) 30 (64%)	28 (97%) 39 (64%)	nd	nd

The table summarizes the characteristics of cMDI tumors. In the case of JA-2017, re-transplanted growth was observed only in SCID/bg but not in syngeneic female mice. Estimated growth times in established models are the mean or range of tumor growth until termination of at least 12 tumor-bearing animals (growth curves) **. In the other established models, growth times were calculated from the outgrowth of frozen or directly * re-transplanted tumor pieces in various experiments. Take rates reflect the percentage of animals developing a tumor within an estimated growth time. Appearance is defined as the earliest time point(s) allowing robust randomization at mean tumor volumes between 40 and 150 mm³ in re-transplanted animals. Intense variation in animal numbers is mostly caused by unexpected death or termination due to ethical reasons. Thus, we defined the so-called real running time (RRT) of the models. RRT determines the time difference from implantation to the time point when the remaining animal number reaches ~60% of the starting animal group size. Thus, it also defines TTW, i.e., the maximal treatment time window to treat animals from randomization (AP) to the potential study end. This allows for calculation of a realistic study length, as well as necessary group size for statistically reliable analysis of, e.g., immune checkpoint inhibitors. Included animals: * resulting from frozen or directly re-transplanted tumor pieces (number of animals), ** growth curves resulting from re-transplantation of frozen tumor pieces into 12 animals each. Bold—growth in another strain only; Grey columns are not yet characterized by growth curves (below-4) or the tumor grows only in another mouse strain (above-1)

Approximately one month later, a growing tumor was detected in the right hind leg of a female CBA/J mouse (JA-2019) which received subcutaneous administration of MCA. During necropsy, an enlarged and strongly vascularized axillary lymph node was also found but not further processed. Re-transplanted frozen tumor tissue grew well between 24 and 35 days in syngeneic mice (Figure 2, Table 2). Another month later, another animal had to be sacrificed due to ethical reasons after a small tumor on the right flank of a female CBA/J mouse (JA-2011) was ulcerated. This mouse received subcutaneous administration of MNU, and the re-transplanted frozen tumor grew between 21–30 days (Figure 2, Table 2). About two weeks later, a fourth tumor was removed from the right hind leg of a male after intramuscular injection of MCA (JA-2042), which grew between 28–35 days (Figure 2, Table 2).

In the following months, three other cMDI tumors were detected (Figure 2, Table 2). They were established from a male animal with subcutaneous MNU treatment (JA-2034), a female mouse with subcutaneous MCA treatment (JA-2017), and a male CBA/J mouse with subcutaneous MCA treatment (JA-2043) with growth between 29 and 55; 14 and 28; and 17 and 36 days, respectively (Figure 2, Table 2). The latter showed invasive growth into the peritoneal wall with massive vascularization (Doc. S1-cMDI). In contrast to other cMDIs, the primary JA-2017 tumor did grow after re-transplantation but only in immunodeficient SCID/bg and not in syngeneic mice (similar to JA-0021 sMDI [1]). This was also the case for SCID/bg-derived, re-transplanted daughter tumors, e.g., 1573-16 (Figure 2, Table 2).

During a total observation time of about 10 months, eight carcinogen-induced ($2 \times$ MNU, $6 \times$ MCA) cMDI tumors were finally established, i.e., a stable re-transplantation into syngeneic or immunodeficient (SCID/bg) recipients could be performed using frozen tumor pieces. In most cases, localized cMDI tumors were induced, and only in some cases were suspicious tissues detected. Carcinogen induction (carcinogen and route), animal number, sex, tumor types, and general growth characteristics of all established cMDI models, as well as general histopathological diagnoses (see below), are summarized in Table 2 and Figure 2, Doc. S1-cMDI.

Additionally, tumors or suspicious tissues were detected, and the primary isolates were re-transplanted in nine other mice (s.c. MNU ♀, s.c. MCA ♀, s.c. MCA ♀, p.o. MCA ♀, p.o. MCA ♀, i.p. MNU ♂, p.o. MNU ♂, p.o. MNU ♂, and p.o. MNU ♂). The tumor and tissue pieces were stored frozen until further use. Thus, carcinogen treatment ($5 \times$ MNU, $4 \times$ MCA) by various routes ($3 \times$ s.c., $5 \times$ p.o., $1 \times$ i.p.) induced malignant growth in a total of 17/28 (i.e., 25 alive) mice. However, in the latter nine cases a stable outgrowth of potential frozen cMDI samples must be verified as the basis for further development.

2.2. cMDI—Histological and Pathological Analysis

To characterize the pathological phenotypes of cMDI and to verify the phenotypic stability of tumor tissue after several rounds of re-transplantation, hematoxylin and eosin (HE) staining of the tissue was performed. For this purpose, primary isolates (tumor or suspicious tissue/s) and derived follow-up subcutaneous re-transplants were compared. Photographs of the primary in situ location, typical HE stains of tumor tissues, and primary diagnoses are shown in Figure 2. In contrast to heterogeneous tumorigenicity in spontaneous sMDI models (ADC, HAL/HS, and lymphomas), only one cMDI tumor was characterized as a spinocellular carcinoma, whereas all other established tumors were identified as sarcomas. Single models are described below. More detailed histopathological characterization, as well as larger microphotographs of various cMDI models, are shown in the Supplementary Data (Doc. S1-cMDI). In addition, a preliminary assessment of the histological analysis of the host stroma reaction and inflammatory response, including the tumor-infiltrating leukocyte index, is shown for some of the models (Doc. S1-sMDI). These findings were confirmed and refined by flow cytometry and RNA-Seq analysis of cMDI JA-2011, JA-2019, JA-2041, or JA-2042 (see below). These first four cMDI models were also used to determine take rates, growth curves, and to perform the first efficacy studies (see below).

JA-2011/0242-17: NOS (not otherwise specified) sarcoma composed of spindle-shaped elongated cells (neoplastic mesenchymal cells) with numerous giant mononuclear or multinucleate giant cells.

The tumor is deeply invasive of adjacent tissues. The re-transplanted tumor 0242-17 contains more “anaplastic cells”, hallmark of a more anaplastic “aggressive” sarcoma than the index case (Figure 2, Doc. S1-cMDI–page 4 ff).

JA-2019/0174-17: NOS storiform sarcoma composed of interwoven bundles of spindle-shaped elongated cells (neoplastic mesenchymal cells) with minimum anaplasia and clearer and denser areas. They are deeply invasive in both skeletal muscle and adipose tissue (Figure 2, Doc. S1-cMDI–page 8 ff).

JA-2041/1607-16: NOS sarcoma composed of interlacing bundles of alternating longitudinal and transverse bundles or long well-differentiated spindle-shaped cells. There is no ischemic necrosis in the tumor of the index case. The homogenous sarcomatous tissue is infiltrating the skeletal muscles. Neoplastic cells exhibit low pleomorphism but have relatively numerous infiltrating lymphocytes and deeply invade into atrophic muscle fibers (Figure 2, Doc. S1-cMDI–page 11 ff). The derived established case 1607-16 depicted shows ischemic necrosis indicative of inadequate vascularization, indicative of cancer progression, and with numerous infiltrating lymphocytes.

JA-2042/0124-17: NOS sarcoma with hemangiosarcoma-like differentiation composed of interwoven bundles of spindle-shaped elongated cells with plump nuclei, minimum anaplasia, and clearer and denser areas. Both the source and established tumor either invades adjacent to blood vessels eliciting vascular ectasia or exhibits vascular differentiation, mimicking a hemangiosarcoma. The index tumor also has rare spaces related to single cell degeneration (Figure 2, Doc. S1-cMDI–page 14 ff). Notice the excellent phenotypic stability in most of these four tumor samples. The tumor invades the skeletal muscle, and its likely origin is the integument of the leg.

JA-2034/0125-17: NOS sarcoma index case JA-2034 developed within the adipose tissue of the panniculus, which is diffusely invaded by bundles of spindle-shaped cells. The tissue is well-differentiated and of moderate anaplasia. The tissue site of invasion is hypodermis (panniculus). Ischemic necrosis is absent. Neoplastic cells exhibit moderate pleomorphism (no bizarre anaplastic cells) and numerous small infiltrating lymphocytes. The established derived tumor features an increased degree of anaplasia, more mitoses, with a few bizarre giant cells (green arrows) and evidence of limited early ischemic necrosis, indicative of inadequate vascularization and thus selection of more aggressive cells (Figure 2, Doc. S1-cMDI–page 17 ff).

JA-2043/0074-17: NOS sarcoma with varying aspects from well-differentiated to moderately anaplastic; no giant cells and weak to moderate leukocyte infiltration. It is deeply invading the skin up to the upper dermis. The tissue shows many anaplastic features (abnormal mitoses, large vesicular nuclei) but no giant multinucleate cells and good phenotypic stability (Figure 2, Doc. S1-cMDI).

JA-2044/1418-16: Interestingly, all other established cMDI tumors were identified as sarcomas. Only JA-2044 and follow-up tumors were characterized as spinocellular (epidermoid) carcinoma, which is an epithelial neoplastic proliferation from the skin characterized by epidermal differentiation and keratin production. It induces intense inflammation with a pronounced lymphoid component as well as fibrosis. It is characterized by cords and nodular elements of keratinocytes with central laminar keratinization, often forming central cysts with occasional horn pearls. The neoplasm entraps a nerve. The majority of the tumor sections examined is composed of desmoplastic and highly inflamed stroma (Figure 2, Doc. S1-cMDI–page 25 ff). It exhibits good phenotypic stability.

JA-2017/1573-16: NOS sarcoma varying from well-differentiated to moderately anaplastic; no giant cells. In contrast to the other cMDIs, re-transplanted JA-2017 tumors grow only in SCID/bg, but not in the syngeneic CBA/J strain. However, the diagnosis is identical for both the primary CBA/J and the secondary SCID/bg tumor (Figure 2, Doc. S1-cMDI–page 28 ff). Both invaded intracutaneously and peritoneally, with weak to moderate leukocyte infiltration. The established derived tumor exhibits multiple small foci of necrosis, whereas the index tumor does not, indicative of a more aggressive neoplasm (tumor progression).

2.3. cMDI—Take Rates and Growth Curves

After model establishment, i.e., a stable outgrowth of frozen tumor pieces, growth curves, and take rates of such transplanted tumor pieces were determined in four cMDI models, JA-2011, JA-2019, JA-2041, and JA-2042 (Table 2, Figure 3). Mean growth times and take rates of the four other models were calculated from the outgrowth of frozen or directly re-transplanted tumor pieces (Table 2).

Comparing growth curves of the four models, JA-2011, JA-2019, JA-2041, and JA-2042, showed variable tumor growth periods of 14–35, 16–63, 25–105, and 25–46 days, and take rates varying from 83%–100% (Table 2, Figure 3) *appearance*, i.e., the earliest time point(s) allowing robust randomization at mean tumor volumes between 40 and 150 mm³ in the 12 (or less, depending on the take rate) animals are varying, from 10 to 12; 4 to 7; 7 to 11; and 9 to 13 days, respectively (Table 1, Figure 3). However, the resulting observation period and *treatment time window (TTW)* were not simply the difference between *appearance* and the determined tumor growth period. Since a varying quantity of animals in single tumor models had to be sacrificed due to fast tumor growth or ulcerations (ethics), or were found dead for unknown reasons, the number of animals still alive had already critically decreased before the end of the growth periods. Therefore, we defined the so-called *real running time* of the models. *RRT* determines the time difference from implantation to the time point when the remaining animal number reaches ~60% of the starting animal group size.

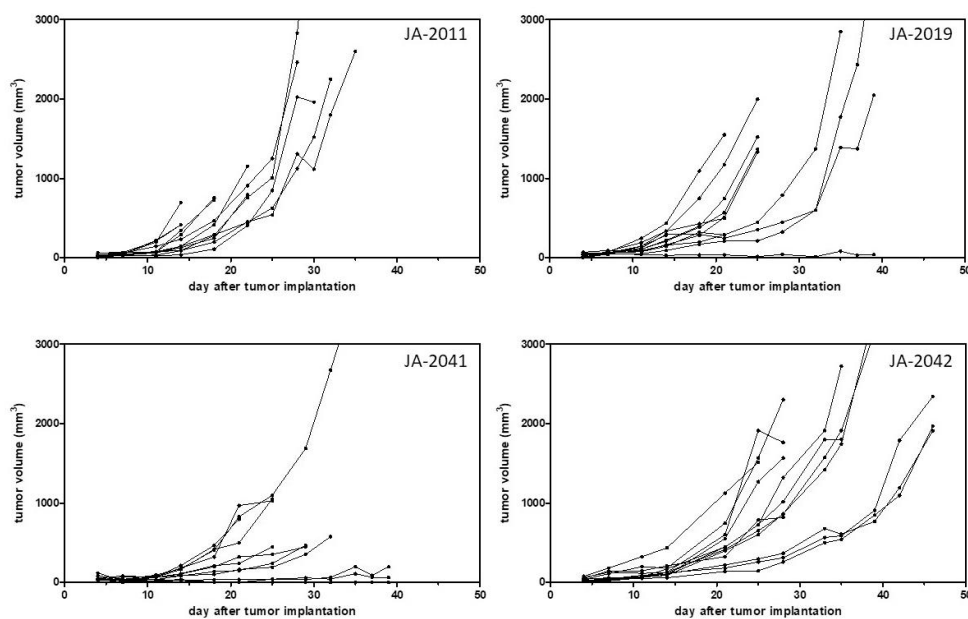


Figure 3. Take rates and growth curves of four cMDI models. Growth curves of 10–12 mice each implanted with frozen tumor pieces are shown. Tumor growth was measured twice weekly by calipering.

Thus, it also defines *TTW*, i.e., the maximal time range to treat animals after randomization (*AP*) to the potential study end. This allows for calculation of a realistic study length as well as necessary group size for statistically reliable analysis for testing, e.g., immune checkpoint inhibitors. For the four cMDI sarcoma models, we outlined potential study endpoints, with *RRTs* (and actual *TTWs*) of about 22–30 (12–18), 21–25 (17–18), 25–30 (18–19), or 28–39 (19–26) days (Table 2).

The models showed not only variable growth periods but also varying growth properties. A heterogeneous growth could be observed in the case of three of the four characterized models, JA-2019, JA-2041, and JA-2042 (Figure 3). Only tumor JA-2011 showed more homogeneous growth, but in this model, individual tumor-bearing animals were also lost by ulceration and, later, by fast tumor growth (ethics). In the three other models, a few tumors were slow-growing, while other tumors grew fast or rather moderately. It remains unclear whether these variations in tumor growth reflected differences between re-transplanted tumor pieces or between individual mice, or were caused by chance.

Individual mice of selected models were chosen for further analysis by flow cytometry (JA-2011, JA-2019, JA-2041, and JA-2042), as well as RNA-Seq analysis (JA-2011 and JA-2042). Additionally, enough animals could be included for efficacy studies to investigate antitumor treatment effects in the four cMDI models (see below).

Hence, to also apply the other established cMDI models, e.g., to perform efficacy studies, the exact growth curves and take rates still need to be determined.

2.4. cMDI—Flow Cytometric Analysis of Tumor-Infiltrating Leukocytes

Material of re-transplanted and outgrown cMDI was isolated and processed for flow cytometry to analyze various populations of tumor-infiltrating leukocytes. Single cell suspensions were stained with master antibody mixes (T cell panel, myeloid cell panel, macrophage cell panel). The results of flow cytometric analysis for cMDI JA-2011, JA-2019, JA-2041, and JA-2042 are shown in Figure 4A. A quantitative comparison of intratumoral immune cell populations of various cMDI is shown in Figure 4B. Comparing these results with former flow cytometric analyses of seven syngeneic standard in vivo mouse models, MC38-CEA, CT26.WT, LL/2, Clone M3, 4T1, RENCA, or B16.F10 (for details of the models—Figure S2—sMDI), most striking differences were seen regarding a massive infiltration of CD4⁺ lymphocytes (~3-fold higher) in cMDI JA-2019, JA-2041, and JA-2042, but not in cMDI JA-2011 (Figure 4B). Regarding other immune cell populations (CD8⁺, M1 and M2 macrophages, neutrophils, and M-MDSC), the four models were in the same range as standard syngeneic mouse models but with striking individual variations. However, in Treg cells, an enhanced (2–3-fold) invasion was seen in JA-2019 and JA-2042. Another exception is the 3-fold enhanced invasion of M1 macrophages into JA-2041 and a 1.5-fold higher number of neutrophils found in JA-2011 tumors (Figure 4B).

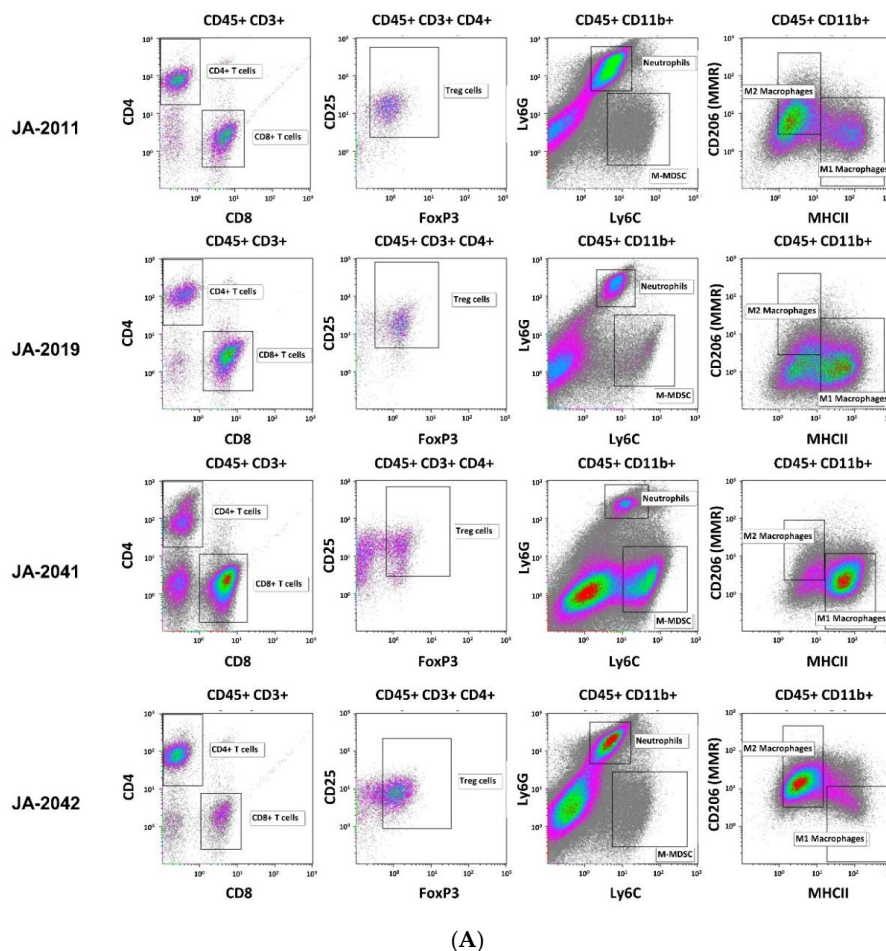


Figure 4. Cont.

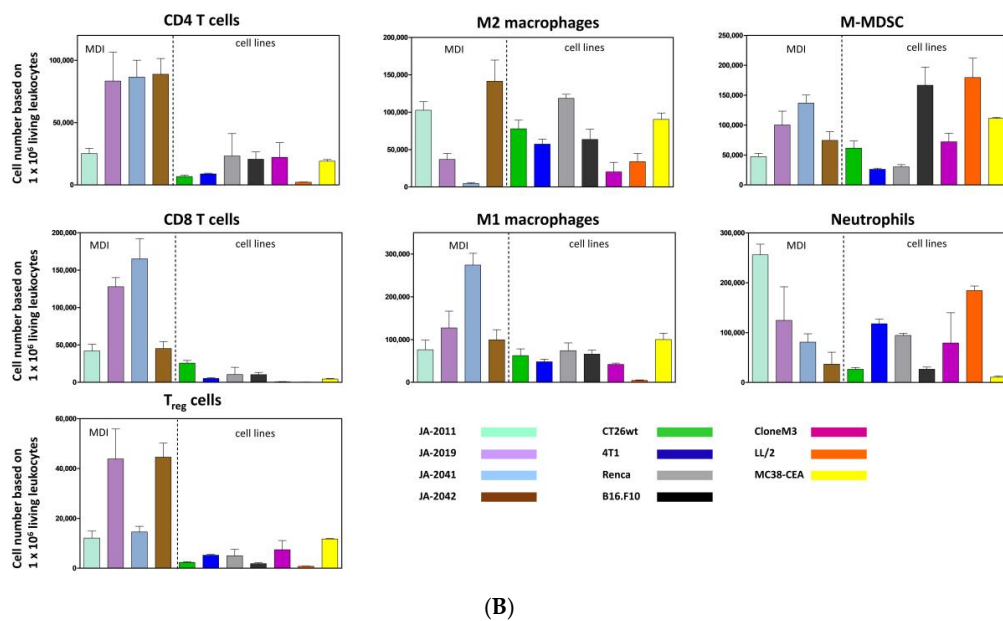


Figure 4. (A). Flow cytometric analysis of cMDI tumor-infiltrating leukocytes. Representative flow cytometry plots of tumor-infiltrating CD4⁺ and CD8⁺ T-cells, T reg cells, M-MDSCs, neutrophils/G-MDSC (cells of CD11b⁺, Ly6G⁺, Ly6C^{int} phenotype), and M1/M2 macrophage populations isolated from untreated syngeneic cMDI tumors JA-2011, JA-2019, JA-2041, and JA-2042. M-MDSC = monocytic myeloid-derived suppressor cells, MMR = macrophage mannose receptor, Treg = regulatory T-cells. (B). Quantitative flow cytometric analysis of cMDI tumor-infiltrating leukocytes. Flow cytometry analysis of tumor-infiltrating immune cells (quantitative analysis) in untreated syngeneic cMDI sarcoma JA-2011, JA-2019, JA-2041, and JA-2042 models and seven established syngeneic cell line-based mouse models of CD4⁺/CD8⁺ T-cells, M-MDSCs, neutrophils, M1/M2 macrophage, and Treg cell populations isolated from untreated tumor tissue. The graphs depict the number of cells of each population per 1×10^6 living leukocytes. For further information regarding depicted syngeneic established cell line-derived standard tumors and experimental details, see Figure S2-sMDI, and Doc. S2-sMDI of the accompanying paper [1].

2.5. cMDI—Preliminary Results of RNA-Seq

A comparison of RNA-Seq analysis of sMDI JA-0009, as well as cMDI JA-2011 and JA-2042, was performed, and details are shown in the Supplementary Data of the accompanying paper [1]. RNA-Seq analysis was mainly conducted to obtain an overview on target expression for potential new drug development and to identify potential mutations. Additionally, complete RNA-Seq whole transcriptome shotgun sequencing analysis will provide a further tool to localize tumor tissue origin.

In the first step, expression profiles of various genes of three gene families related to tumor malignancy or antitumor immune response were created: tyrosine kinase receptors, immune population markers, and IFN- γ signature, which comprises multiple interferon-responsive genes involved in innate and adaptive immune activities (see accompanying paper [1]).

A direct comparison between individual MDI models was not possible, since FPKM (fragment per kilobase million) values were not determined in simultaneous experiments. However, indirect comparison of individual gene expression based on an internal, low expression reference gene (Table S1a–c-sMDI, Figure S1 a_{i-iii}-sMDI, and Figure S1 b_{i-iii}-sMDI) [1] shows very different individual gene expression patterns of the two histologically related cMDI sarcomas (JA-2011 and JA-2042). Whether this reflects tumor induction by different routes (s.c. versus i.m.) and carcinogens (MNU versus MCA) remains unclear. The RNA-Seq data further support and confirm findings already obtained by other methods. For example, RNA-Seq displayed enhanced Cd4 gene expression in JA-2041 (Table S1a–c-sMDI, Figure S1 a_{i-iii}-sMDI, and Figure S1 b_{i-ii}-sMDI and inserts), which confirmed flow

cytometry data regarding actual enhanced CD4⁺ T cell tumor infiltration in this cMDI. The details are shown in the Supplementary Data of the accompanying paper [1]. A more complete characterization of gene expression of the whole transcriptome shotgun sequencing analysis of further gene families, as well as in further sMDI and cMDI tumor models, will be the matter of subsequent investigations.

2.6. cMDI—Efficacy Studies

For further characterization of cMDI models, four efficacy studies were performed using various anti-ICPI antibodies. In a first study, animals implanted with JA-2011 tumor pieces were randomized on day 13 into groups of 12 animals each.

Starting on the day of randomization, animals were treated three times (dotted lines) with anti-mPD-1 antibody or anti-mCTLA-4, as shown in Figure 5. Neither anti-mPD-1 nor anti-mCTLA-4 showed significant effects on tumor growth.

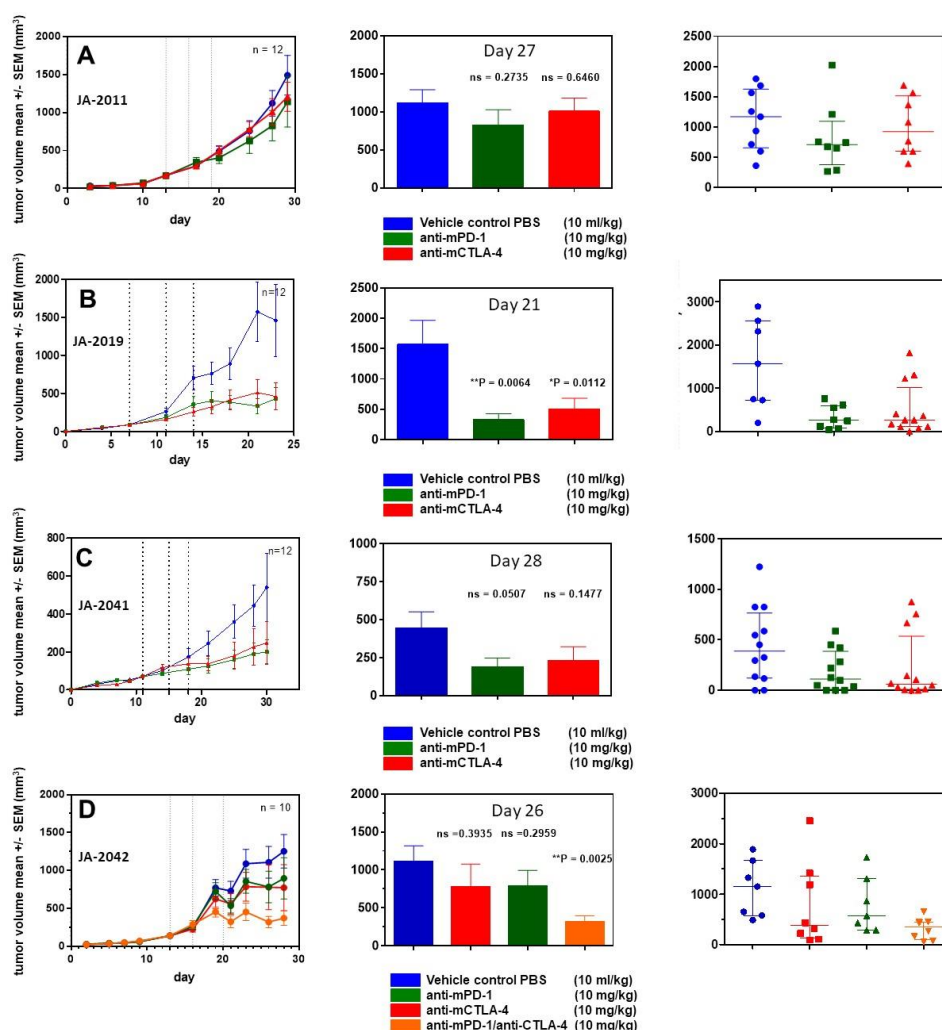


Figure 5. Efficacy studies of selected cMDI models using immune checkpoint inhibitor antibodies. Efficacy of immune checkpoint inhibitor antibodies (anti-PD-1, anti-CTLA-4, or combinations thereof) was investigated in four selected cMDI models (A) JA-2011, (B) JA-2019, (C) JA-2041, and (D) JA-2042. Ten to 12 sex-matched CBA/J mice per group were treated three times (details of treatment schedule—see Material and Methods) with antibodies or PBS as vehicle control (dotted lines). Results are shown as mean (curve and bar graphs) and individual values of single mice (dot plots) with standard error of the mean (SEM). Probability (*p*) was tested with a parametric unpaired *t* test (GraphPad Prism 5.04) as compared to PBS vehicle control. Differences were determined as not significant with *ns* > 0.050 and significant * with *p* < 0.050, ** with *p* < 0.010, or *** with *p* < 0.001.

In a second study, JA-2019 tumor pieces were implanted, and mice were randomized on day 7 into groups of 12 mice each. Starting on the day of randomization, mice were treated in a similar schedule with anti-ICPI antibodies. In contrast to JA-2011, a tumor inhibitory effect was induced, which was significant for anti-mPD-1 (** $p = 0.0064$) as well as anti-mCTLA-4 (* $p = 0.0112$) on day 21.

In a third study, JA-2041 tumor pieces were implanted, and randomization took place on day 11. At randomization day, the first treatment with anti-mPD-1 and anti-mCTLA-4 was performed. Although both antibodies reduced tumor growth by about 50% after three treatments, none of the effects were significant when compared on day 30. Interestingly, anti-mCTLA-4-treated tumors showed a very diverse responses: 9 out of 12 tumors displayed reduced tumor volume by about 80–90%, whereas the other tumors did not show any response. It is unclear whether this reflects actual differences between re-transplanted tumor pieces or between individual mice, or is caused by other reasons.

In a fourth efficacy study, using JA-2042 tumor pieces, we were interested in the possible effects of anti-mPD-1, anti-mCTLA-4, or a combination of both antibodies, which may amplify or induce tumor inhibitory effects [9]. After randomization on day 13, groups of 10 mice were treated as described above. The antibody combination led to a significant reduction (** $p = 0.0025$) of tumor volume on day 26. Both single treatments with anti-mPD-1 and anti-mCTLA-4 moderately reduced tumor volume by about 25%, which was not significant. The anti-mCTLA-4 monotherapy seems to result in two effects: strong tumor growth inhibition in a part (5/10) of the tumors, and no effect in others (3/10), similar to the observations within the JA-2041 and JA-2019 tumor models.

3. Discussion

The new MDI *in vivo* cancer models display a model quality and properties unavailable with standard syngeneic tumor models and are therefore closer to actual clinical situation in patients [1]. sMDIs represent outgrowing spontaneous tumors (or metastases) which have overcome the body's own regulatory mechanisms, as already introduced in the accompanying paper. They are transplantable, i.e., "single step" tumorigenic not only in the primary tumor-bearing animal, but also in other syngeneic, fully immunocompetent hosts without any prior or subsequent additional *in vivo* or *in vitro* manipulation [1].

Here, we established syngeneic carcinogen-induced mouse-derived isograft (cMDI) models from once subcutaneously, intravenously, intramuscularly, intraperitoneally, or three times orally with MCA or MNU injected, otherwise untreated, CBA/J mice of both sexes (Table 1). The general characteristics of cMDI are similar to those of sMDI tumors, i.e., primary tumors of low passage number were propagated only *in vivo* as tissue pieces in syngeneic mice (in a PDX-like manner), resulting in rather conserved tumor characteristics and tumor-infiltrating immune cell populations [1]. However, in contrast to sMDI, the animals for cMDI development have been manipulated by carcinogen treatment to induce tumor growth. The resulting cMDI differ histopathologically from sMDI tumors. Whereas sMDI comprise adenocarcinomas, lymphomas, or histiocytic sarcoma/histiocyte-associated lymphomas [1], the predominant tumor entities of cMDIs were sarcomas. In addition, one spinocellular carcinoma model could be established.

These new models increase the number of available syngeneic tumor models. However, one cMDI model, JA-2017, did grow in immunodeficient SCID/bg mice only. Therefore, it seems to be not a "true" CBA/J H-2^k model. However, histologic characterization indicates that both primary and secondary tumors are of the same origin, since it displays an identical diagnosis of well to moderately differentiated anaplastic sarcoma. Hence, the most suitable explanation for growth restricted to immunocompromised SCID mice might be because that JA-2017 tumor is highly immunogenic, resulting in a rejection of tissue transplanted into syngeneic immunocompetent mice. This should be verified, e.g., by specific immunosuppression in immunocompetent mice. It is well known that carcinogen-induced tumors are often more immunogenic than spontaneous tumors [10], mostly caused by the expression of TATA [5–7]. Thus, the occurrence of just one tumor with high immunogenicity

in the present study was rather surprising. In other cases, e.g., of MCA-induced fibrosarcomas in rats, 75% of the animals displayed TATA antigen expression and showed stronger immunogenicity [8]. In the case of chemically induced lung tumorigenesis and antigen expression, though, strain-specific differences were found with high tumor susceptibility in A/J mice and with intermediate susceptibility in BALB/c mice, whereas C57BL/6N or DBA/2N mice resisted carcinogen treatment (reviewed in [3]). For various immunotherapeutic approaches, it would be very interesting to identify if TATA antigens were present in cMDI models [11]. The observed striking invasion by CD4⁺ and/or CD8⁺ lymphocytes in 3 of 4 CBA/J cMDI models (except for JA-2011) seems to be a first indicator of such an enhanced immunogenicity and the presence of TATA in carcinogen-induced tumors (Figure 4B). In this context, it must be clarified why this does not lead to immediate tumor rejection (Figure 3) or to higher sensitivity to anti-ICPI antibody immunotherapy (Figure 5A–D). The overall effects of the anti-mPD-1 or anti-mCTLA-4 antibody monotherapies could be divided into “non-responder” (JA-2011), “moderate responder” (JA-2041 and JA-2042), as well as “responder” (JA-2019) models. Except for JA-2011, the reactivity pattern was very similar (Figure 5). In “moderate responder” and “responder” models, anti-mPD-1 caused a homogeneous individual tumor growth reduction, whereas anti-mCTLA-4 nearly completely inhibited the growth of tumors in all three models, but in only about 60% to 70% of the mice (Figure 5B–D). The monotherapies led merely in JA-2019 (“responder”) to a general and significant tumor growth inhibition by each of the two antibodies (Figure 5B). Nevertheless, there was no explanation for the resistance of certain cMDI to anti-mCTLA-4 or anti-mPD-1 monotherapies either within all (JA-2011) or single individual mice (JA-2041, JA-2042) in the other models (Figure 5A,C,D). However, the rather unexpected complete inhibition of tumor growth in all mice, observed by combined treatment with both anti-mPD-1 and anti-mCTLA-4 antibodies in JA-2042 (Figure 5D), might be a first indication of how to overcome the problem. Results showed that JA-2042 cMDI tumors basically display sufficient immunogenicity to become completely inhibited. However, considering present studies, it remains unclear whether the varying effects in individual mice relate to different properties (e.g., antigenic pattern) of individual tumor pieces or mirror a varying immune status of individual syngeneic mice, and if they caused by a combination of both, or by chance, or an unknown mechanism. Thus, in future, the outcome of such a combinatorial effect must also be investigated in the other cMDI models.

The resistance of “non-responder” model JA-2011 to anti-ICPI treatment seems to display another phenomenon. JA-2011 showed the fastest and most homogeneous growth of the four investigated cMDI models. Compared to the other anti-mCTLA-4 sensitive models, JA-2011 displayed a different pattern of tumor-infiltrating leukocyte populations, with a low infiltration of lymphocytic CD4⁺ and CD8⁺ effector cells, and many neutrophils (Figure 4B). This could be the explanation for the bad prognosis and tumor-supporting conditions, as well as for the low or missing antibody response [2,12,13]. On the other hand, JA-2011 was the only MNU-induced tumor, whereas the other tumors were induced by MCA. Former studies have shown that different carcinogens could induce carcinogen-specific mutations, which might then differentially activate various oncogenes and affect progression to malignancy [14]. Additionally, various carcinogens may also differ in their ability to transform the one or the other cell type [15] and, as already mentioned above, strain-specific differences in carcinogen susceptibility [3] might also influence the experimental outcome. In contrast, the data do not provide any evidence what might cause the resistance to antibody treatment e.g., in ICPI non-responder JA-2011.

The first RNA sequencing data regarding the expression of tyrosine kinase receptors, IFN- γ -signature or immune cell population markers, showed various patterns comparing the “non-responder” JA-2011 and “moderate responder” JA-2042 models (Table S1a–c-sMDI, Figure S1 a_{i–iii}-sMDI, and Figure S1 b_{i–iii}-sMDI and inserts [1]). The relationship of expression patterns between individual models demonstrates very different gene expression patterns between two related cMDI sarcomas (JA-2011 and JA-2042). It remains unclear if the differences might be caused by different routes (s.c. versus i.m.) or carcinogens (MNU versus MCA) used for induction, and if they are

also related to the different response patterns. Flow cytometry confirmed that enhanced Cd4 gene expression in JA-2042 was actually associated with enhanced CD4⁺ T cell infiltration by various tumor-infiltrating leukocytes. To assess this question, future studies need to be performed to characterize the gene expression of further gene markers, such as immune cell-specific genes [2] or tumor-specific genes [16], and compare these with the gene expression in respective primary human samples [17]. In addition, this analysis should be extended to further established sMDI and cMDI tumors.

The establishment of the MDI models opens a door for the better understanding of tumor antigenicity, conditions, potential signals, and the role of tumor infiltration by immune cells and their relation to response to therapeutic interventions. The various outcomes and questions regarding MDI models of, e.g., possible tumor subgroups, histological heterogeneity, individual TATA, and varying sensitivity to treatment, remains unresolved, since this was not the matter of the exemplary present investigations. In the present two papers, we introduced new mouse-derived isograft models and described their establishment, characteristics, and potential for future research.

It can be assumed that the MDI model variety will be further enhanced by establishing cMDI and sMDI in additional inbred mouse strains with immunological differences [18–21], but also genetically heterogeneous in angiogenesis [22], with various susceptibility to drugs [23], or with varied strain-specific susceptibility for metastasis [24].

To sum up, we can state that MDI models are promising and effective *in vivo* cancer research tools. They reflect the clinical situation better than other *in vivo* mouse tumor models. cMDI and sMDI models allow for comparison of new therapeutic concepts against either specific tumor entities or different MHC backgrounds. Thus, the combination of the two model types will be more suitable and relevant for studying the interactions between stroma, immune cells, and tumor environment in cancer progression, metastasis, and therapy in a completely natural host.

4. Materials and Methods

4.1. Mouse Strains

All *in vivo* experiments were performed in accordance with the German Animal License Regulations (Tierschutzgesetz), identical to UKCCCR Guidelines for the welfare of animals in experimental neoplasia (license: G-15/160; Regierungspräsidium Freiburg) [25]. CBA/J mice at 12 weeks of age from Charles River Laboratories, Sulzfeld, Germany were used for all studies. Mice were housed under pathogen-free conditions in conventional cages stored in Scantainer ventilated cabinets, Scanbur, Denmark, with autoclaved nesting material, and cardboard tunnels. Mice were housed on a 12/12 h light/dark cycle, with *ad libitum* autoclaved water and M-Zucht rodent diet, ssniff Spezialdiäten GmbH, Soest, Germany. Four animals were housed in one cage; however, if any animals exceeded 30 g body weight during the observation period, just 2–3 animals were housed within one cage.

4.2. Monitoring of Animals

Animal weights were measured twice weekly during observations and three times weekly during the treatment studies (balance: Mettler Toledo PB602-L). Animal behavior was monitored daily.

Termination criteria: If the volume of tumors exceeded 2000 mm³ or an edge length of 2 cm, tumor ulcerations, weight loss of >20%, cachectic phenotype (tumor cachexia), remarkably abnormal, non-physiological posture as a sign of pain, apathy (severe inactivity), strongly reduced feed and water intake, severe dyspnea, motor deficit manifestations or paralysis, ascites, persisting diarrhea, massive behavioral changes, or other unexpected signs were observed, indicating an obviously heavy burden of the animals, the mice would be immediately sacrificed, according to the ATBW/GV-SOLAS.

4.3. Carcinogen Induction of Tumor Growth

To establish primary cMDI tumors, animals were treated once subcutaneously, intravenously, intramuscularly, intraperitoneally, or 3 times orally with either 3-methylcholanthrene (MCA) or *N*-methyl-*N*-nitrosourea (MNU) (Sigma-Aldrich Chemie GmbH, Steinheim, Germany) followed by short-term (3–9-month) monitoring for tumor appearance. The animals were treated according to the following schemes (Table 1): Group one—four female mice were treated subcutaneously on the right and left flank (s.c.) and once additionally into one intramammary fat pad (imfp) with 50 mg/kg MNU per injection in sterile 0.85% NaCl (pH 5.0). Four male mice of this group were also injected s.c. and once intravenously (i.v.); Group two—four male mice (3 animals died within 2 days after injection for an unknown reason) were treated once intraperitoneally (i.p.) with 100 mg/kg MNU in DMSO (Sigma-Aldrich Chemie GmbH, Steinheim, Germany) [26–29]; Group three—four male and female mice each were treated once s.c. with 0.1 mL (5 mg/mL) MCA in sesame oil (Sigma-Aldrich Chemie GmbH, Steinheim, Germany) and once additionally with 0.025 mL intramuscularly (i.m.) on the right hind leg [30,31]; Group four—four male and female mice each were orally (p.o.) treated 3 times in weekly intervals with 0.3 mL of an MCA emulsion (5 mg/mL) in sesame oil [32].

When animals met termination criteria, the handling of tumors or any suspicious tissue was done in the same way as described already for spontaneous ones [1]. Briefly, tumors and suspicious tissues were assessed macroscopically and cut into small pieces (of 2 to 3 mm³) in sterile PBS using a scalpel. The tumor pieces were either stored in 10% DMSO freezing medium at ≤ -80 °C or directly implanted s.c. into 5- to 6-week-old sex-matched syngeneic and/or female immunodeficient SCID/bg mice using a trocar. Two hours prior to transplantation, mice received the analgesic Meloxicam (Metacam®; 1 mg/kg, Boehringer Ingelheim Vetmedica GmbH, Ingelheim, Germany) s.c. Implantation was performed under anesthesia with 2 to 3 volume percent isoflurane in combination with an oxygen flow rate of 0.6 L/min. Primary tumor volumes were determined by caliper measurement two times a week. Tumor sizes were calculated according to the formula $W^2 \times L/2$ (L = length and W = the perpendicular width of the tumor, $L > W$).

4.4. Mouse-Derived Isograft (cMDI) Re-Transplantation

Frozen tumor pieces were thawed rapidly at 37 °C and washed twice in ice-cold PBS, and then implanted as described above. The growth of transplanted tumor pieces was observed until termination criteria were met. During necropsy, tumor tissue but also other suspicious tissues were collected (F1). To amplify the number of tumor pieces derived from one primary tumor, tumor pieces were generated and re-transplanted again into mice (F2). Excess of tumor pieces were frozen stored at ≥ -80 °C or in the vapor phase of liquid nitrogen.

Amplification and sample collection were repeated several times, and samples were called F1–Fn ($n = F3$ –6 amplifications) [33]. Some tumor pieces (primary and re-transplanted) were fixed in formalin for further analysis. The model development was finished by successful re-transplanting and testing the outgrowth of frozen tumor pieces into 4 to 6 syngeneic animals.

4.5. cMDI—Histological and Pathological Analysis

Wet tissues were collected in embedding cassettes and formalin-fixed in 4% neutral buffered formaldehyde (Engelbrecht, Edermünde, Germany) at room temperature for about 24 h, followed by automatic dehydration and embedding in IHC-grade paraffin using a Leica TP 1020 (Leica Biosystems, Nussloch, Germany) and Leica Histo Core Arcadia H/C (Leica Biosystems). FFPE tissue blocks were stored at room temperature. Sections from paraffin blocks with non-specified tissues were cut into slices of approximately 2–3 μ m thickness and routinely stained with HE at TPL Path Labs (Freiburg, Germany).

Histopathological examinations were then performed blind using a Zeiss Axioscope microscope (Carl Zeiss, Jena, Germany) at a magnification of up to 400 \times , by one of the authors (T.L.). Digital

microphotographs were taken using a Nikon Digital Sight DS-Fi camera (Nikon Instruments Europe B.V., Amsterdam, Netherlands). Whole slide imaging using an Axioscan Z1 (Carl Zeiss) were also performed from all case, for the purpose of comprehensive iconography.

4.6. cMDI—Establishment and Efficacy Studies

To assess growth curves as well as take rates of cMDI, frozen tumor pieces were transplanted into 12 sex-matched animals. In the following, animals were monitored as described above. Deviation of the health status was documented, and animals were euthanized individually before study termination when ethical termination criteria were met. Take rate was defined as the percentage of total tumor-bearing versus all animals during the observation period. From primary re-transplanting studies, it is known that in some cases, animals could also develop tumors later, but this growth was not included in the analysis. *Real running time* ascertains the actual number of live tumor-bearing animals at study end. This number of animals may be smaller than defined by take rates, since animals could be lost by fast tumor growth (i.e., termination by tumor volume), were repeatedly found dead for unknown reasons, or were lost by unexpected ulcerations (termination for ethical reasons) before the end of the observation period. Determination of *appearance* denotes the time range at which randomization of a sufficiently large number of animals with tumor growth is possible, and whose tumor properties (e.g., volumes, growth rate) must be appropriately taken into consideration for randomization criteria. For randomization, a robust automated random number generation within individual blocks was used (MS-Excel 2016, Microsoft, Redmond, WA 98052, USA). Both *appearance* and *real running time* allow for defining how many animals must be implanted with tumor pieces to randomize about 10–12 animals per group at *appearance*, which will also still be alive at the end of the observation period.

Treatment was initiated on the day of randomization, according to the following schedules: vehicle control (PBS) and anti-ICPI antibodies (anti-mPD-1, anti-mCTLA-4, or combination of anti-mPD-1/anti-mCTLA-4) were injected i.p. 3 times every third or fourth day (Q3d3/4x), with a dosage of 10 mg/kg and an injection volume of 10 mL/kg (combination 5 mL/kg). Tumor growth and effects regarding tumor growth reduction due to therapeutic intervention were followed by caliper measurement until the end of observation. The study was finalized by necropsy, tumors were resected, and tumor volumes and wet weights in the experimental groups were determined and documented. In some cases, parts of tumors from various experimental groups were also formalin-fixed and paraffin-embedded, and used for flow cytometry analysis and/or RNA sequencing. Probability (*P*) was tested with a parametric unpaired *t* test (GraphPad Prism 5.04, GraphPad Software, San Diego, CA 92108, USA) compared to PBS vehicle control. Differences were determined as not significant with $n_s > 0.050$ and as significant * with $p < 0.050$, ** with $p < 0.010$, and *** with $p < 0.001$.

4.7. Flow Cytometric Analysis of cMDI Tumor-Infiltrating Leukocytes

Primary tumor material (at least approx. 300 mg) was disrupted using gentleMACS™ C Tubes (Miltenyi Biotec, Bergisch Gladbach, Germany) containing the enzyme mix of the Tumor Dissociation Kit (mouse) according to the manufacturer's instructions (Miltenyi Biotec). Following that, erythrocytes were removed with the Red Blood Cell Lysis Solution (Miltenyi Biotec). The obtained single cell suspensions were counted and dispensed in two 96-well plates, if possible, at 3×10^6 cells/well (if there were, in total, less than 2×10^6 single cells in a tumor sample, the T cell panel was preferred for staining). The single cells were washed with PBS (Capricorn, Ebsdorfergrund, Germany) and stained for living cells using eBioscience™ Fixable Viability Dye (Thermo Fisher, Nidderau, Germany). After washing and centrifugation (400 g), the samples were incubated with 50 μ L/well Fc block (anti-mouse CD16/CD32, 1:50) for 30 min in FACS buffer. Thereafter, a 2 \times concentrated master antibody mix (T cell panel with antibodies against murine CD45, CD3, CD4, CD8a, CD25, CD44, myeloid cell panel with antibodies against murine CD45, CD11b, CD11c, Ly6G, and Ly6C, and macrophage panel CD45, CD11b, F4/80, MHC II, CD206) was added to each well (50 μ L) and incubated for 30 min in the dark.

After washing, cells stained for the myeloid or macrophage cell panel were fixed. Cells stained for the T cell panel were prepared for intracellular staining. Intracellular staining was primed by adding 50 µL fix/perm (Thermo Fisher Scientific) buffer for 30 min. Thereafter, 1 × permeabilization buffer was added and centrifuged at 836 g. The cell pellet was resuspended in 1 × permeabilization buffer containing the anti-FoxP3 antibody and incubated for 30 min in the dark. After two times washing with 1 × permeabilization buffer, cells were washed with FACS™ buffer. The cells were kept at 4 °C in the dark until analysis, no later than 5 days after preparation. The samples were analyzed by flow cytometry using an BD LSR Fortessa™ (Becton Dickinson, Heidelberg, Germany). All antibodies were purchased from Thermo Fisher except for CD3 and CD206 (BioLegend, San Diego, CA 92121, USA), and CD8a (Becton Dickinson).

4.8. cMDI—RNA-Seq

For details on RNA-Seq whole transcriptome shotgun sequencing analysis, please see the accompanying paper [1].

5. Conclusions

The established MDI models described in the two related papers are a new type of promising *in vivo* cancer testing tools representing primary spontaneous [1] or carcinogen-induced tumors of a low passage number that are propagated in mice only, without any tissue culturing. Therefore, the models possess conserved tumor characteristics and intratumoral immune cell populations, which were histologically and genetically characterized. Carcinogen-induced tumors established in this way represent outgrowing tumors (or metastases) which have overcome the body's own regulatory mechanisms, and are thus comparable to clinically manifest tumors, without any previous or further *in vivo* or *in vitro* manipulation. Since chemical induction resulted mostly in sarcomas, therapeutic effects in various tumors of similar origin can be investigated. The first results indicated that individual tumors—despite their relatedness—might differ in their therapeutic sensitivity.

Future inclusion of other mouse strains with different MHC classes and immunological backgrounds will enhance the therapeutic window. If not be restricted to only one MHC class and immunological archetype, the models will correspond to experiments in various “individuals” but with the possibilities to repeat or vary treatment concepts. Additionally, further refinement of the established models will be possible. Use of relapsing tumors from original ones after various kinds of treatments (immunological, chemotherapeutic, irradiation, or combinations thereof) also open possibilities to search and find follow-up concepts for re-treating therapy-resistant relapsing tumors.

Together, this opens a broader field of experimental *in vivo* cancer therapeutic concepts.

Supplementary Materials: The following are available online at <http://www.mdpi.com/2072-6694/11/2/242/s1>, manuscript-supplementary.pdf; Doc. S1-cMDI: cMDI—Histological and Pathological Analysis: This document summarizes detailed histopathological analysis of primary and derived tumors of various cMDI models and includes their respective large microphotographs.

Author Contributions: P.J. conceived of the MDI studies (spontaneous and carcinogen-induced), P.J. and C.O. designed the animal experimental application, P.J., C.S. and H.W. designed the experimental setup, P.J., J.B. and H.W. performed the animal experiments, C.O. performed the veterinary monitoring, T.L. carried out the histological and pathological analysis, H.W. carried out the inhouse RNA-Seq analysis, J.B. and H.W. performed Flow Cytometry analysis, J.B. and P.J. carried out the establishment and efficacy studies, P.J., J.B., H.W., and C.S. wrote the manuscript, with input from all authors. All authors read and approved the final manuscript.

Funding: The research did not receive external funding. These R&D studies were fully financed by the “ProQinase GmbH”.

Acknowledgments: Thanks to our colleagues Bianca Giesen, Ulrike Leisegang, Sandra Moor, Susanne Ruf, and Gojko Bijelic for their excellent technical support during our work. Special thanks go to Katrin Schlie for critical reading and final editing of the manuscript.

Conflicts of Interest: The “ProQinase GmbH” is the owner and provider of the established MDI models and will also use them for own commercial applications in tumor therapy and for testing new substances or strategies

concomitant with cancer treatment. An MTA-restricted availability of the models for academic investigations and purposes will be possible. All the authors declare that they have no competing individual interests.

Abbreviations

ADC	adenocarcinoma
AP	<i>appearance</i>
bg	beige mutation
cMDI	carcinogen-induced mouse-derived isografts
CRL	Charles River Laboratories
DMSO	Dimethyl sulfoxide
FACS	fluorescence activated cell sorter
FPKM	fragments per kilobase million
HS/HAL	histiocytic sarcoma//histiocyte-associated lymphoma
ICPI	immune checkpoint inhibitors
IFN	interferon
IRE	internal relative expression
LN	lymph node
MCA	3-methylcholanthrene
mCTLA-4	mouse cytotoxic T-lymphocyte-associated protein 4
MDI	Mouse-derived isografts
MDSC	myeloid-derived suppressor cells
MHC	major histocompatibility complex
M-MDSC	monocytic MDSC
MMR	macrophage mannose receptor
MNU	N-methyl-N-nitrosourea
mPD-1	mouse programmed cell death protein 1
NOD mice	non-obese diabetic mice
NOS	not otherwise specified
NSG mice	NOD SCID gamma mice
PBS	phosphate-buffered saline
PDX	patient-derived xenografts
RNA	ribonucleic acid
RNA-Seq	RNA whole transcriptome shotgun sequencing
RPKM	reads per kilobase million
RRT	<i>real running time</i>
SCID	severe combined immunodeficiency disease
SCID mice	severe combined immunodeficiency mice
SCID/bg	SCID beige mutation
SCID/bg mice	severe combined immunodeficiency beige mice
TATA	tumor-associated transplantation antigens
Treg	regulatory T-cells
TTW	<i>treatment time window</i>
UKCCCR	United Kingdom Coordinating Committee of Cancer Research

References

1. Jantschkeff, P.; Beshay, J.; Lemarchand, T.; Obodozie, C.; Schächtele, C.; Weber, H. New mouse-derived isograft (MDI) tumor models. Spontaneously appearing sMDI models for immune as well as other therapeutic approaches. *Cancers* **2019**, in press.
2. Mosely, S.I.; Prime, J.E.; Sainson, R.C.; Koopmann, J.O.; Wang, D.Y.; Greenawalt, D.M.; Ahdesmaki, M.J.; Leyland, R.; Mullins, S.; Pacelli, L.; et al. Rational selection of syngeneic preclinical tumor models for immunotherapeutic drug discovery. *Cancer Immunol. Res.* **2017**, *5*, 29–41. [[CrossRef](#)] [[PubMed](#)]

3. Jennings-Gee, J.E.; Moore, J.E.; Xu, M.; Dance, S.T.; Kock, N.D.; McCoy, T.P.; Carr, J.J.; Miller, M.S. Strain-specific induction of murine lung tumors following in utero exposure to 3-methylcholanthrene. *Mol. Carcinog.* **2006**, *45*, 676–684. [[CrossRef](#)] [[PubMed](#)]
4. Nci Dictionary of Cancer Terms: Solid Tumor. Available online: <https://www.cancer.gov/publications/dictionaries/cancer-terms/def/solid-tumor> (accessed on 16 February 2019).
5. Foley, E.J. Antigenic properties of methylcholanthrene-induced tumors in mice of the strain of origin. *Cancer Res.* **1953**, *13*, 835–837. [[PubMed](#)]
6. Klein, G.; Sjogren, H.O.; Klein, E.; Hellstrom, K.E. Demonstration of resistance against methylcholanthrene-induced sarcomas in the primary autochthonous host. *Cancer Res.* **1960**, *20*, 1561–1572. [[PubMed](#)]
7. Prehn, R.T.; Main, J.M. Immunity to methylcholanthrene-induced sarcomas. *J. Natl. Cancer Inst.* **1957**, *18*, 769–778. [[PubMed](#)]
8. Baldwin, R.W.; Embleton, M.J.; Pimm, W.V. Tumour rejection antigens associated with carcinogen-induced tumours. In *Tumor-associated Antigens and Their Specific Immune Response*; Spreafico, F., Arnon, R., Eds.; Academic Press: London, UK; New York, NY, USA; San Francisco, CA, USA, 1979; p. 21.
9. Mangsbo, S.M.; Sandin, L.C.; Anger, K.; Korman, A.J.; Loskog, A.; Totterman, T.H. Enhanced tumor eradication by combining ctla-4 or pd-1 blockade with cpg therapy. *J. Immunother.* **2010**, *33*, 225–235. [[CrossRef](#)]
10. Basombrio, M.A.; Prehn, R.T. Immune status of autochthonous and adoptively protected mice toward spontaneous and chemically induced tumors. *Cancer Res.* **1972**, *32*, 2545–2550.
11. Matsushita, H.; Vesely, M.D.; Koboldt, D.C.; Rickert, C.G.; Uppaluri, R.; Magrini, V.J.; Arthur, C.D.; White, J.M.; Chen, Y.S.; Shea, L.K.; et al. Cancer exome analysis reveals a t-cell-dependent mechanism of cancer immunoediting. *Nature* **2012**, *482*, 400–404. [[CrossRef](#)]
12. Coffelt, S.B.; Kersten, K.; Doornebal, C.W.; Weiden, J.; Vrijland, K.; Hau, C.S.; Verstegen, N.J.M.; Ciampricotti, M.; Hawinkels, L.; Jonkers, J.; et al. Il-17-producing gammadelta T cells and neutrophils conspire to promote breast cancer metastasis. *Nature* **2015**, *522*, 345–348. [[CrossRef](#)]
13. Wculek, S.K.; Malanchi, I. Neutrophils support lung colonization of metastasis-initiating breast cancer cells. *Nature* **2015**, *528*, 413–417. [[CrossRef](#)]
14. Brown, K.; Buchmann, A.; Balmain, A. Carcinogen-induced mutations in the mouse c-ha-ras gene provide evidence of multiple pathways for tumor progression. *Proc. Natl. Acad. Sci. USA* **1990**, *87*, 538–542. [[CrossRef](#)]
15. Gunning, W.T.; Castonguay, A.; Goldblatt, P.J.; Stoner, G.D. Strain a/j mouse lung adenoma growth patterns vary when induced by different carcinogens. *Toxicol. Pathol.* **1991**, *19*, 168–175. [[CrossRef](#)]
16. Julien, S.; Merino-Trigo, A.; Lacroix, L.; Pocard, M.; Goere, D.; Mariani, P.; Landron, S.; Bigot, L.; Nemati, F.; Dartigues, P.; et al. Characterization of a large panel of patient-derived tumor xenografts representing the clinical heterogeneity of human colorectal cancer. *Clin. Cancer Res.* **2012**, *18*, 5314–5328. [[CrossRef](#)]
17. Li, A.; Walling, J.; Kotliarov, Y.; Center, A.; Steed, M.E.; Ahn, S.J.; Rosenblum, M.; Mikkelsen, T.; Zenklusen, J.C.; Fine, H.A. Genomic changes and gene expression profiles reveal that established glioma cell lines are poorly representative of primary human gliomas. *Mol. Cancer Res.* **2008**, *6*, 21–30. [[CrossRef](#)]
18. Belzung, C.; Barreau, S. Differences in drug-induced place conditioning between balb/c and c57bl/6 mice. *Pharmacol. Biochem. Behav.* **2000**, *65*, 419–423. [[CrossRef](#)]
19. Chen, X.; Oppenheim, J.J.; Howard, O.M. Balb/c mice have more cd4+cd25+ t regulatory cells and show greater susceptibility to suppression of their cd4+cd25- responder t cells than c57bl/6 mice. *J. Leukoc. Biol.* **2005**, *78*, 114–121. [[CrossRef](#)]
20. Melgar, S.; Karlsson, A.; Michaelsson, E. Acute colitis induced by dextran sulfate sodium progresses to chronicity in c57bl/6 but not in balb/c mice: Correlation between symptoms and inflammation. *Am. J. Physiol. Gastrointest. Liver Physiol.* **2005**, *288*, G1328–G1338. [[CrossRef](#)]
21. Tucker, C.F.; Nebane-Ambe, D.L.; Chhabra, A.; Parnell, S.A.; Zhao, Y.; Alard, P.; Kosiewicz, M.M. Decreased frequencies of cd4+cd25+foxp3+ cells and the potent cd103+ subset in peripheral lymph nodes correlate with autoimmune disease predisposition in some strains of mice. *Autoimmunity* **2011**, *44*, 453–464. [[CrossRef](#)]
22. Rohan, R.M.; Fernandez, A.; Udagawa, T.; Yuan, J.; D’Amato, R.J. Genetic heterogeneity of angiogenesis in mice. *FASEB J.* **2000**, *14*, 871–876. [[CrossRef](#)]

23. Marmiroli, P.; Riva, B.; Pozzi, E.; Ballarini, E.; Lim, D.; Chiorazzi, A.; Meregalli, C.; Distasi, C.; Renn, C.L.; Semperboni, S.; et al. Susceptibility of different mouse strains to oxaliplatin peripheral neurotoxicity: Phenotypic and genotypic insights. *PLoS ONE* **2017**, *12*, e0186250. [[CrossRef](#)]
24. Vikis, H.G.; Jackson, E.N.; Krupnick, A.S.; Franklin, A.; Gelman, A.E.; Chen, Q.; Piwnica-Worms, D.; You, M. Strain-specific susceptibility for pulmonary metastasis of sarcoma 180 cells in inbred mice. *Cancer Res.* **2010**, *70*, 4859–4867. [[CrossRef](#)] [[PubMed](#)]
25. Workman, P.; Balmain, A.; Hickman, J.A.; McNally, N.J.; Rohas, A.M.; Mitchison, N.A.; Pierrepoint, C.G.; Raymond, R.; Rowlatt, C.; Stephens, T.C.; et al. Ukcccr guidelines for the welfare of animals in experimental neoplasia. *Lab. Anim.* **1988**, *22*, 195–201. [[CrossRef](#)] [[PubMed](#)]
26. Schleicher, R.L.; Fallon, M.T.; Austin, G.E.; Zheng, M.; Zhang, M.; Dillehay, D.L.; Collins, D.C. Intravenous vs. Intraprostatic administration of n-methyl-n-nitrosourea to induce prostate cancer in rats. *Prostate* **1996**, *28*, 32–43. [[CrossRef](#)]
27. Coburn, M.A.; Brueggemann, S.; Bhatia, S.; Cheng, B.; Li, B.D.; Li, X.L.; Luraguiz, N.; Maxuitenko, Y.Y.; Orchard, E.A.; Zhang, S.; et al. Establishment of a mammary carcinoma cell line from syrian hamsters treated with n-methyl-n-nitrosourea. *Cancer Lett.* **2011**, *312*, 82–90. [[CrossRef](#)]
28. McCormick, D.L.; Adamowski, C.B.; Fiks, A.; Moon, R.C. Lifetime dose-response relationships for mammary tumor induction by a single administration of n-methyl-n-nitrosourea. *Cancer Res.* **1981**, *41*, 1690–1694.
29. Westcott, P.M.; Halliwill, K.D.; To, M.D.; Rashid, M.; Rust, A.G.; Keane, T.M.; Delrosario, R.; Jen, K.Y.; Gurley, K.E.; Kemp, C.J.; et al. The mutational landscapes of genetic and chemical models of kras-driven lung cancer. *Nature* **2015**, *517*, 489–492. [[CrossRef](#)]
30. Creau-Goldberg, N.; Salomon, J.C. Immunotherapy of primary methylcholanthrene-induced mouse tumours by intratumoral bcg. *Br. J. Cancer* **1980**, *41*, 541–552. [[CrossRef](#)]
31. Ligtenberg, M.A.; Cinar, O.; Holmdahl, R.; Mougiakakos, D.; Kiessling, R. Methylcholanthrene-induced sarcomas develop independently from nox2-derived ros. *PLoS ONE* **2015**, *10*, e0129786. [[CrossRef](#)]
32. Andervont, H.B.; Dunn, T.B. Responses of strain dbaf/2 mice, without the mammary tumor agent, to oral administration of methylcholanthrene. *J. Natl. Cancer Inst.* **1953**, *14*, 329–339. [[CrossRef](#)]
33. Rubio-Viqueira, B.; Jimeno, A.; Cusatis, G.; Zhang, X.; Iacobuzio-Donahue, C.; Karikari, C.; Shi, C.; Danenberg, K.; Danenberg, P.V.; Kuramochi, H.; et al. An in vivo platform for translational drug development in pancreatic cancer. *Clin. Cancer Res.* **2006**, *12*, 4652–4661. [[CrossRef](#)] [[PubMed](#)]



© 2019 by the authors. Licensee MDPI, Basel, Switzerland. This article is an open access article distributed under the terms and conditions of the Creative Commons Attribution (CC BY) license (<http://creativecommons.org/licenses/by/4.0/>).

Type of the Paper (Article - Supplementary Data)

Mouse-Derived Isograft (MDI) *in vivo* Tumor Models

II. Carcinogen-Induced cMDI Models: Characterization and Cancer Therapeutic Approaches

- *Supplementary Data* -

Janette Beshay^{1,3a}, **Peter Jantscheff**^{1a*}, **Thomas Lemarchand**², **Cynthia Obodozie**¹, **Christoph Schächtele**¹, **Holger Weber**^{1*}

¹*In vivo* Pharmacology, ProQinase GmbH, Breisacher Str. 117, 79106 Freiburg, Germany, peter.jantscheff@t-online.de; Janette_Beshay@web.de; c.obodozie@proqinase.com; c.schaechtele@proqinase.com; h.weber@proqinase.com

²TPL Pathology Labs, Sasbacher Str. 10, 79111 Freiburg, Germany, lemarchand@tpl-path-labs.com

*Correspondence: peter.jantscheff@t-online.de; phone: +49-7666-913-0396; h.weber@proqinase.com; phone: +49-761-769996-1733

^aPeter Jantscheff and Janette Beshay contributed equally to this work. ³present address JB: Charles River Discovery Research Services Germany GmbH, Am Flughafen 12-14, 79108 Freiburg, Germany

Received: date; Accepted: date; Published: date.

1. Supplementary Data

Suppl_data_cMDI_models – Cancers.docx – containing:

1.1 Doc. S1-cMDI: sMDI - Histological and Pathological Analysis

p 02

The document summarizes detailed histopathological analysis of primary and derived tumors of various cMDI models inclusive respective large microphotographs

1.1 Doc. S1-cMDI: cMDI - Histological and Pathological Analysis

The document summarizes detailed histopathological analysis of primary and derived tumors of various cMDI models inclusive respective large microphotographs

Table of Contents

1.1 Doc. S1-cMDI: cMDI - Histological and Pathological Analysis	2
List of Figures.....	2
JA-2011 cMDI: NOS sarcoma composed of spindle shaped elongated cells.....	4
JA-2019 cMDI: NOS sarcoma - storiform pattern.....	8
JA-2041 cMDI: NOS sarcoma composed of interlacing bundles	11
JA-2042 cMDI: NOS sarcoma with hemangiosarcoma-like differentiation.....	14
JA-2034 cMDI: NOS sarcoma within adipose tissue of the panniculus	17
JA-2043 cMDI: NOS sarcoma with varying aspects from well differentiated to anaplastic.....	20
JA-2044 cMDI: Spinocellular carcinoma (epidermoid carcinoma)	25
JA-2017 cMDI: NOS sarcoma varying from well differentiated to moderately anaplastic; no giant cells	28

Note: c-MDI is “carcinogen-induced Mouse Derived Isografts; NOS is “not otherwise specified”

List of Figures

Figure 1: Localization of tumor/suspicious tissue in tumor JA-2011	4
Figure 2: An example of one of the cutaneous masses, ulcerating the skin and deeply invading the adjacent tissues from index case 2011-16 (#11975 tu).....	4
Figure 3: phenotypically stable sarcoma tumor model: transmitted tumor to mouse 0242-17	5
Figure 4: Established c-MDI tumor 0242-17 from index case 2011-16	6
Figure 5: Comparison of the source 2011-16 (A) and derived 242-17 (B) neoplasms.....	7
Figure 6: Different macroscopic aspects of the tumors JA-2019	8
Figure 7: Low magnification (sub-gross aspects) of the tumor masses: A and C index tumor 2019-16 and B : established daughter tumor 174-17	8
Figure 8: Comparison of the source 2019-16 (A) and the derived 174-17 (B) neoplasms.....	10
Figure 9: Different macroscopic aspects of the tumors JA-2041	11
Figure 10: Chemically-induced neoplasms (study #11975): sarcoma, not otherwise specified, male CBA/J mouse 2041/16, MCA s.c.....	11
Figure 11: Chemically-induced neoplasms (study #11975): sarcoma, not otherwise specified, male CBA/J mouse 1607/16, MCA s.c.....	13
Figure 12: Low magnification (sub-gross aspect) of the tumor masses: A index tumor 2042-16 and B : established daughter tumor 124-17.....	14

Figure 13:	Comparison of different regions of index 2042-16 and derived 124-17	16
Figure 14:	Chemically-induced neoplasms (study #11975): sarcoma, not otherwise specified, male CBA/J mouse 2034/16, MNU s.c.	17
Figure 15:	Chemically-induced neoplasms (study #11975): sarcoma, not otherwise specified, male CBA/J mouse 0125/17, MNU s.c.	18
Figure 16:	Macroscopic aspects of the tumor JA-2043	20
Figure 17:	High magnification aspects of the index tumor 2043-16: anaplastic	20
Figure 18:	Low magnification (sub-gross aspect) of the tumor masses of the index tumor 2043-16	22
Figure 19:	High magnification aspects of the index tumor 2043-16: fusiform aspects.....	23
Figure 20:	Sub-gross and higher views of grafted JA-2043 into 0074-17 mouse. Tissue similarity with top index tumor at these magnifications is striking. N is central ischemic necrosis of the tumor	24
Figure 21:	Chemically-induced neoplasms (study #11975): spinocellular carcinoma, male CBA/J mouse 2044/16, MCA s.c.	25
Figure 22:	Chemically-induced neoplasms (study #11975): spinocellular carcinoma, male CBA/J mouse 1418/16, MCA s.c.	26
Figure 23:	Originator tumor of the JA-2017: 2017-16 (see next page).....	28
Figure 24:	Low magnification aspect of the derived tumor 1573-16 grafted with JA-2017	0
Figure 25:	Tumor 1573-16 : High magnification view of the region in the Green square.....	1
Figure 26 :	Tumor 1573-16: Medium magnification view of the region in the large blue rectangle from figure 24.....	2

JA-2011 cMDI: NOS sarcoma composed of spindle shaped elongated cells

JA-2011/0242-17: NOS sarcoma composed of spindle shaped elongated cells

Figure 1: Localization of tumor/suspicious tissue in tumor JA-2011



Figure 2: An example of one of the cutaneous masses, ulcerating the skin and deeply invading the adjacent tissues from index case 2011-16 (#11975 tu)

The sarcomatous tissue fully invades the dermis and widely dissects out the preexisting dermis (left inset), eliciting focal epidermal hyperplasia and ulceration at tumor center (black arrows). This is one of the 3 fragments examined

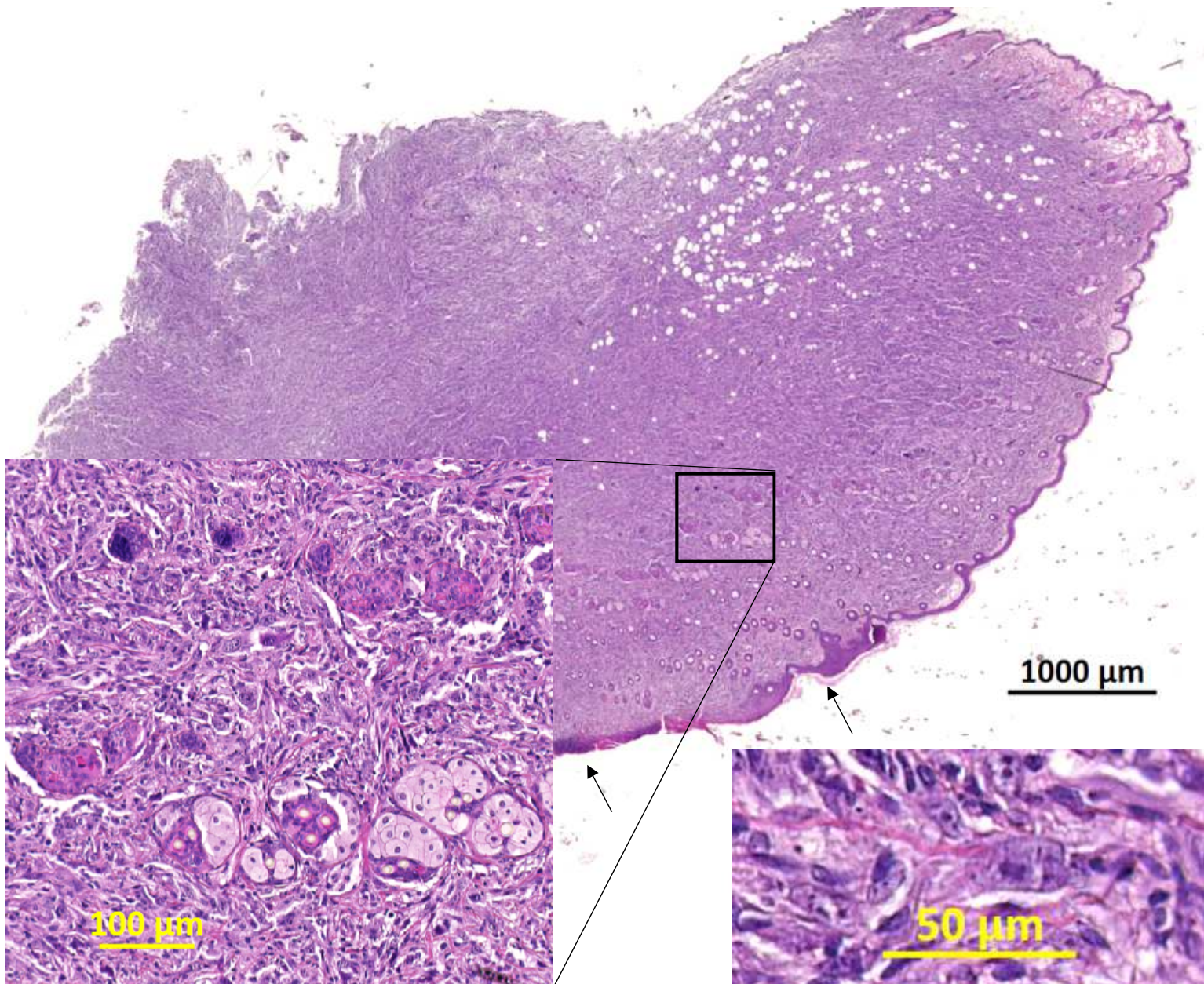


Figure 3: phenotypically stable sarcoma
tumor model:
transmitted
tumor to mouse
0242-17

There is an apparent increase of anaplasia, with the emergence of more numerous (higher density) of large, anaplastic mono-nucleated (red arrow in lower inset) or poly-nucleated giant cells (see the black arrows in insets). See also [Figure 4](#) and [Figure 5](#) narratives on next pages.

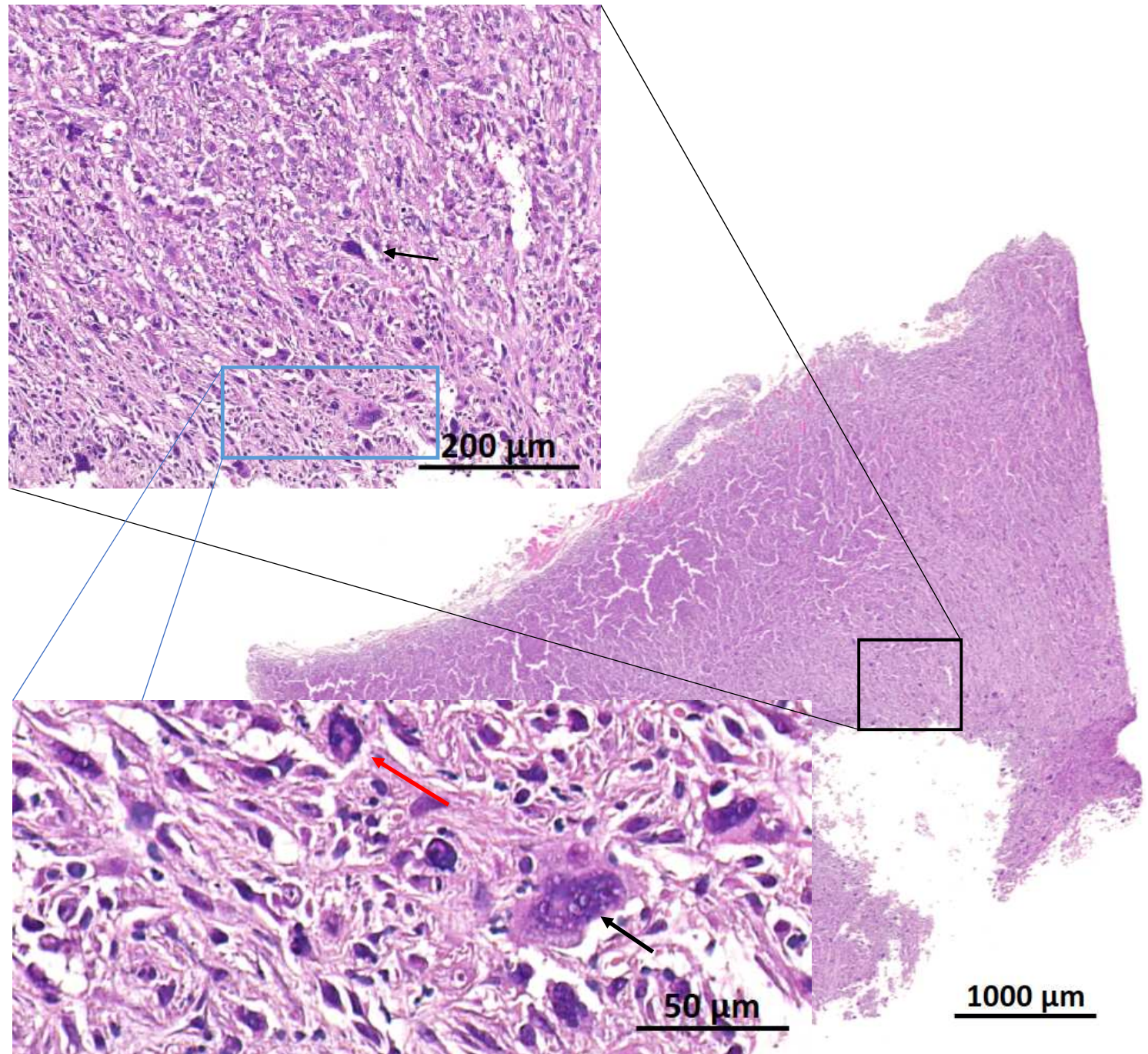
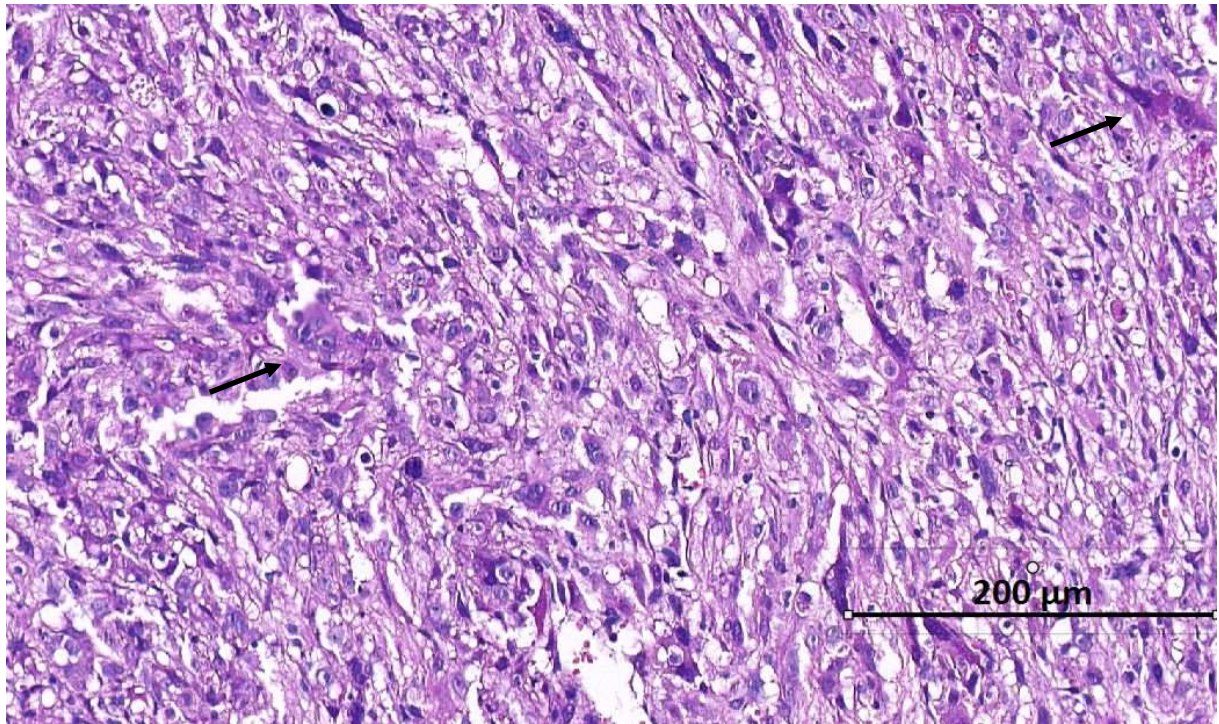


Figure 4: Established c-MDI tumor **0242-17** from index case **2011-16**



Mouse ID #242-17; from index case: mouse ID number 2011-16. Strain CBA/J ♀.

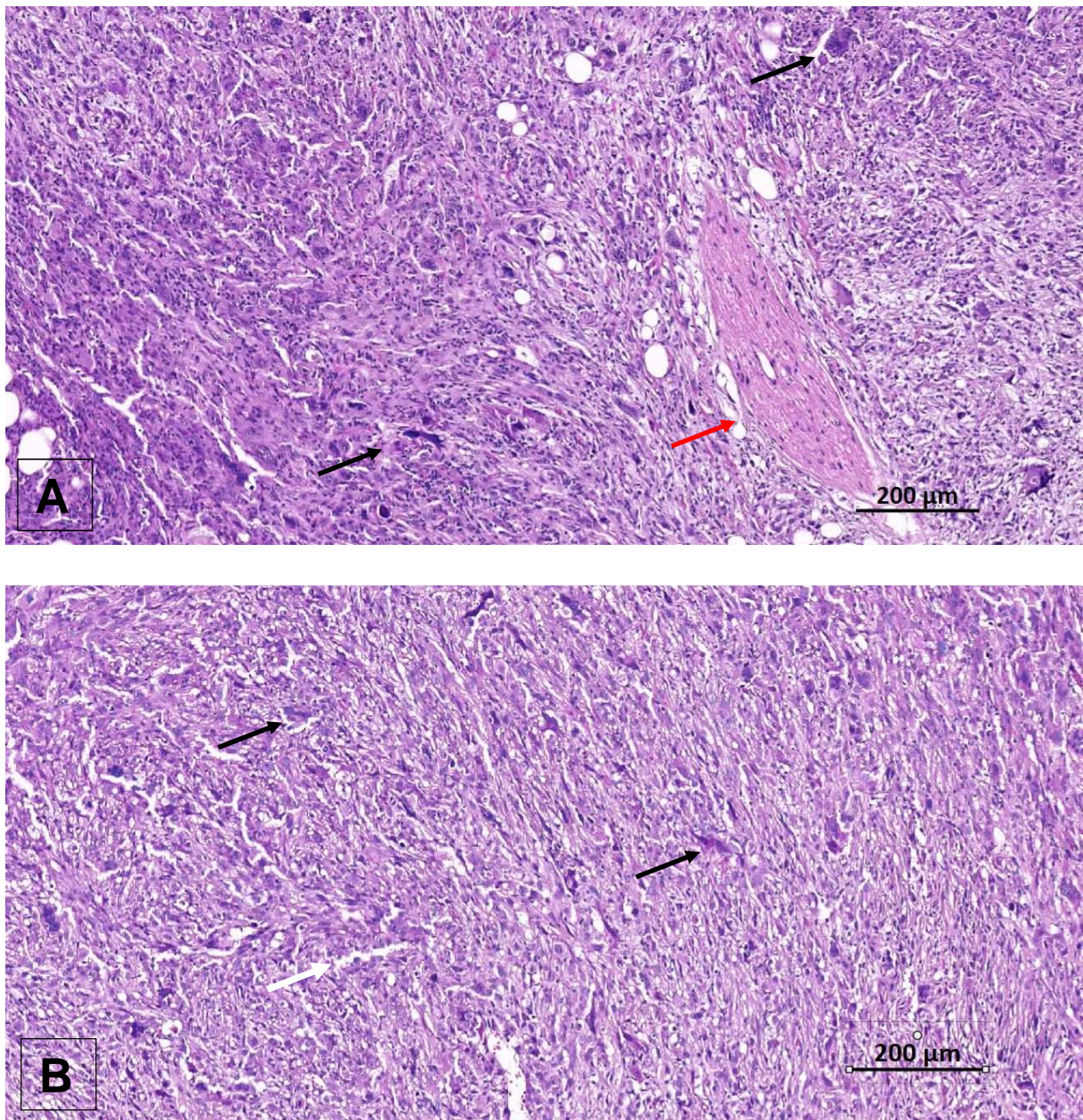
Sarcoma, not otherwise specified (NOS) composed of spindle-shaped, elongated cells (neoplastic mesenchymal cells), with numerous giant mononuclear or multinucleate giant cells or “anaplastic cells” (**black arrows**), suggesting the evolution towards an anaplastic sarcoma. IHC markers could be useful to further characterize this tumor.

Morphological diagnosis: Sarcoma NOS.

Comment: the most common MNU-induced malignant neoplasia

Image source ID: 2017-10-24 17_25_38-12551_242-17___Establish.czi - ZEN 2.3 lite

Figure 5: Comparison of the source **2011-16 (A)** and derived **242-17 (B)** neoplasms



From index case: mouse ID number 2011-16. Strain CBA/J ♀. Induced with MNU.

Sarcoma, not otherwise specified (NOS) composed of spindle shaped elongated cells (neoplastic mesenchymal cells), with numerous giant mononuclear or multinucleate giant cells (**black arrows**), and deeply invasive, in this field invading a host nerve bundle (**A: red arrow**). Notice the remarkable phenotypic stability, at least morphologically with H&E stain, when comparing side by side at matching magnification the index (**A**) and derived (**B**) neoplasms. White arrow: artefactual tissue crack:

A: Image ID: 2017-10-24 17_29_36-11975_tu__2011-16__2011-16.czi - ZEN 2.3 lite – index case (mouse ID) **2011-16**; **B:** image ID: 2017-10-24 17_30_44-12551_242-17__Establish.czi - ZEN 2.3 lite – ID #**242-17**: Extracted from TPL Study Phase Number 780/17

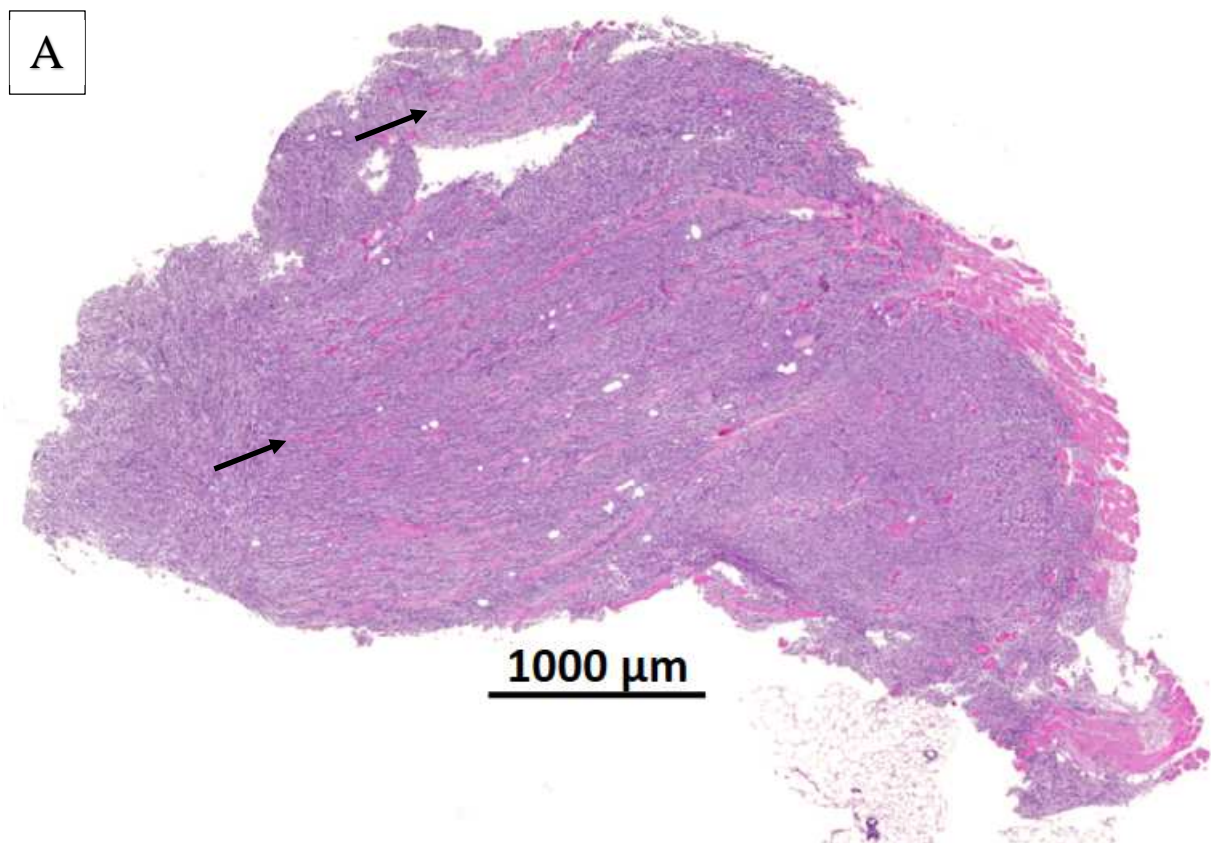
JA-2019 cMDI: NOS sarcoma - storiform pattern

JA-2019/0174-17: NOS sarcoma - storiform pattern composed of interwoven basket weave-like or interlacing bundles of neoplastic spindle-shaped cells

Figure 6: Different macroscopic aspects of the tumors JA-2019



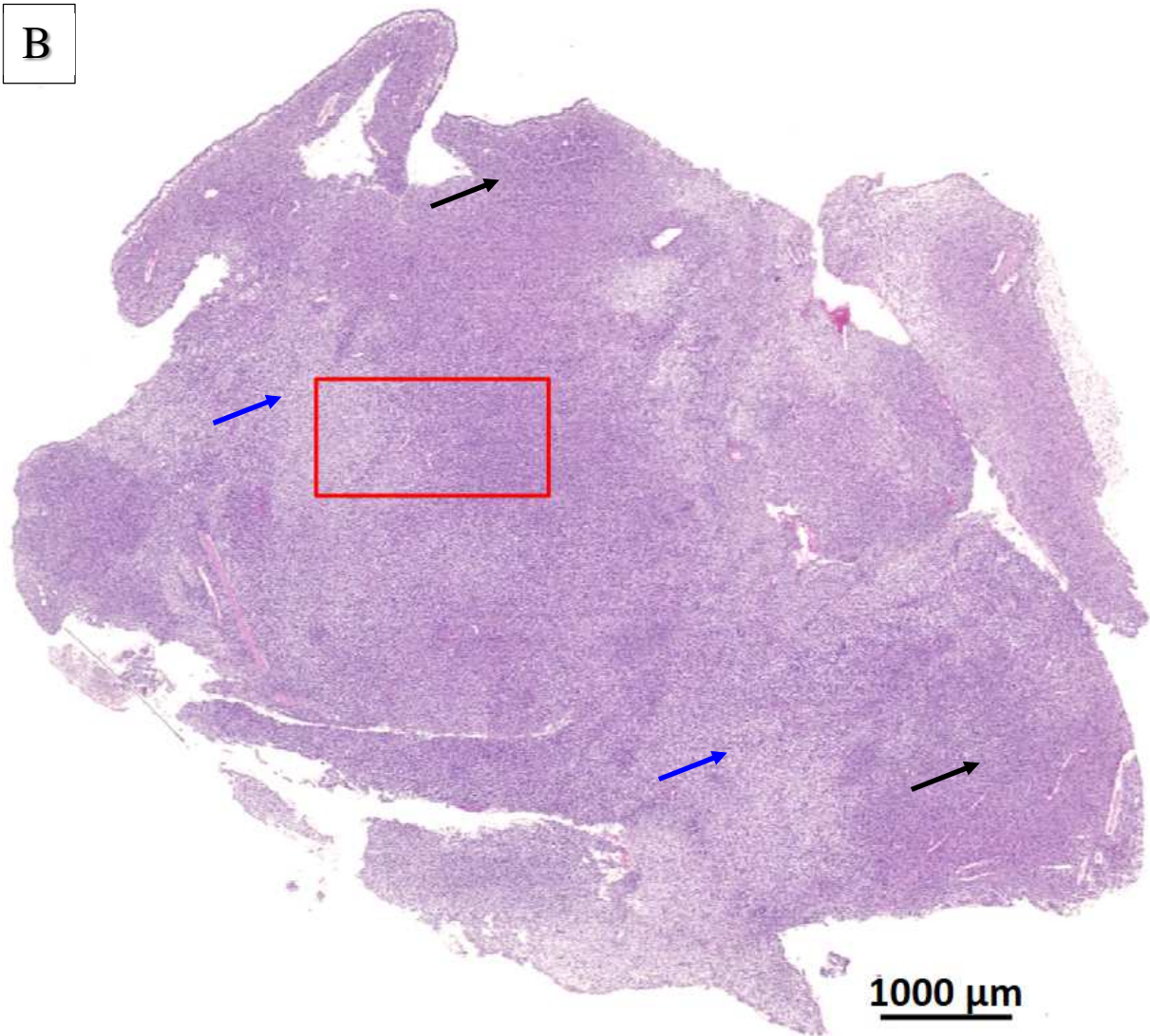
Figure 7: Low magnification (sub-gross aspects) of the tumor masses: **A** and **C** index tumor **2019-16** and **B**: established daughter tumor **174-17**



A: 2019-16: The muscle fibers (**arrows**) are widely separated by bundles of invading sarcomatous tissue, without evidence of any characteristic differentiation.

This is 1 of the 2 fragments submitted. The other fragment is depicted in **C**. Both fragments have a similar morphology

B

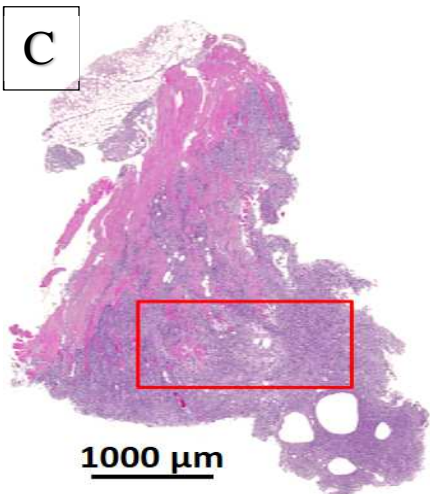


B: Sub-gross view of grafted JA-2019 into 174-17, showing 2 distinct cell density aspects, a higher, more basophilic aspect (**black arrow**) and a lower paler and pinker aspect (**blue arrows**) corresponding to lower cell density with also possibly paler cytoplasm.

The **red rectangle** corresponds to the field depicted in [Figure 8 B](#)

File source: C:\Users\TLEMARCHAND\Documents\ProQinase-Paper-Project\neue bilds\2019-01-24 14_59_17-#12551 174-17.czi - ZEN 2.3 lite.png

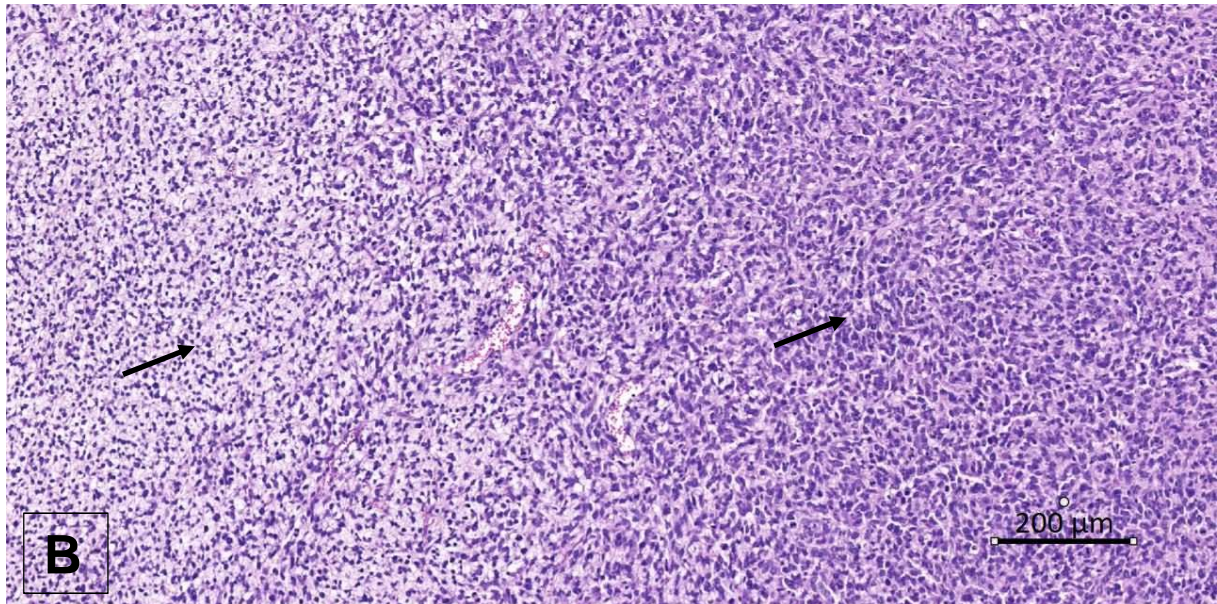
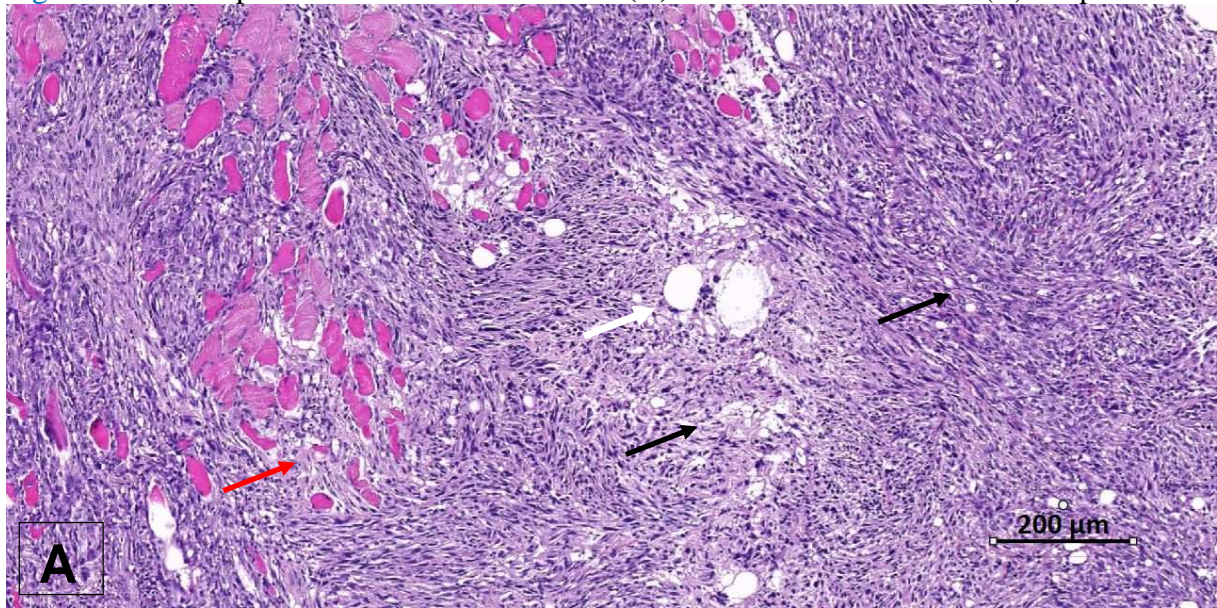
C



C: Sub-gross view of the sarcomatous tissue fully invading the adjacent skeletal muscles. This is one of the 2 fragments (Fragment 2) examined of the index tumor. Fragment 1 is examined in [A](#).

The red rectangle represents the field depicted in [Figure 8 A](#)

Figure 8: Comparison of the source 2019-16 (A) and the derived 174-17 (B) neoplasms



From index case: mouse ID number 2019-16. Strain CBA/J ♀. Induced with MCA. Sarcoma, not otherwise specified (NOS) composed of interwoven bundles of spindle-shaped elongated cells (neoplastic mesenchymal cells), with minimum anaplasia and clearer and denser areas (**black arrows**). They are deeply invasive, in both skeletal muscle (**A: red arrow**, inducing fiber atrophy) and adipose tissue (**A: white arrow**). Notice the relative phenotypic stability, at least morphologically with H&E stain, when comparing side by side the index (**A**) and derived (**B**) neoplasms.

A: Image ID: 2017-10-24 17_32_11-11975_tubein__2019-16__2019-16.czi - ZEN 2.3 lite – index case (mouse ID) 2019-16; **B:** image ID: 2017-10-24 17_32_57-12551_174-17__Establish.czi - ZEN 2.3 lite.jpg – derived tumor ID #174-17: Extracted from TPL Study Phase Number 780/17

JA-2041 cMDI: NOS sarcoma composed of interlacing bundles

JA-2041/1607-16: NOS sarcoma composed of interlacing bundles

Figure 9: Different macroscopic aspects of the tumors JA-2041

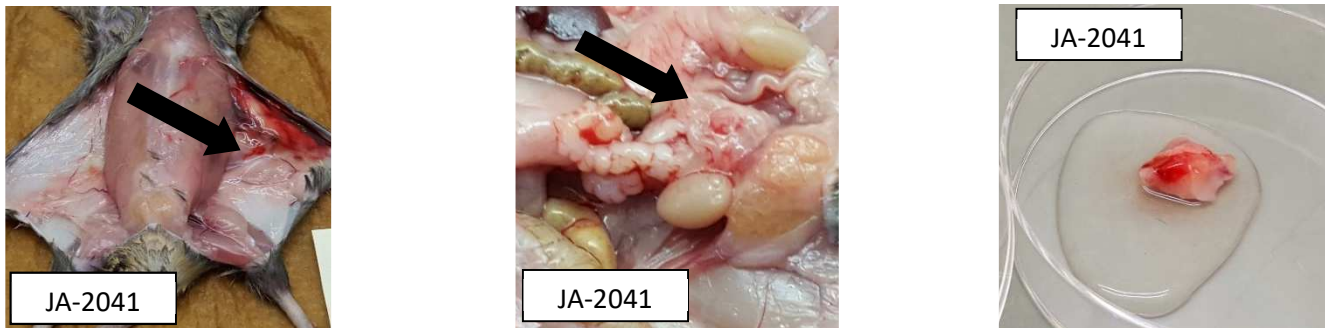
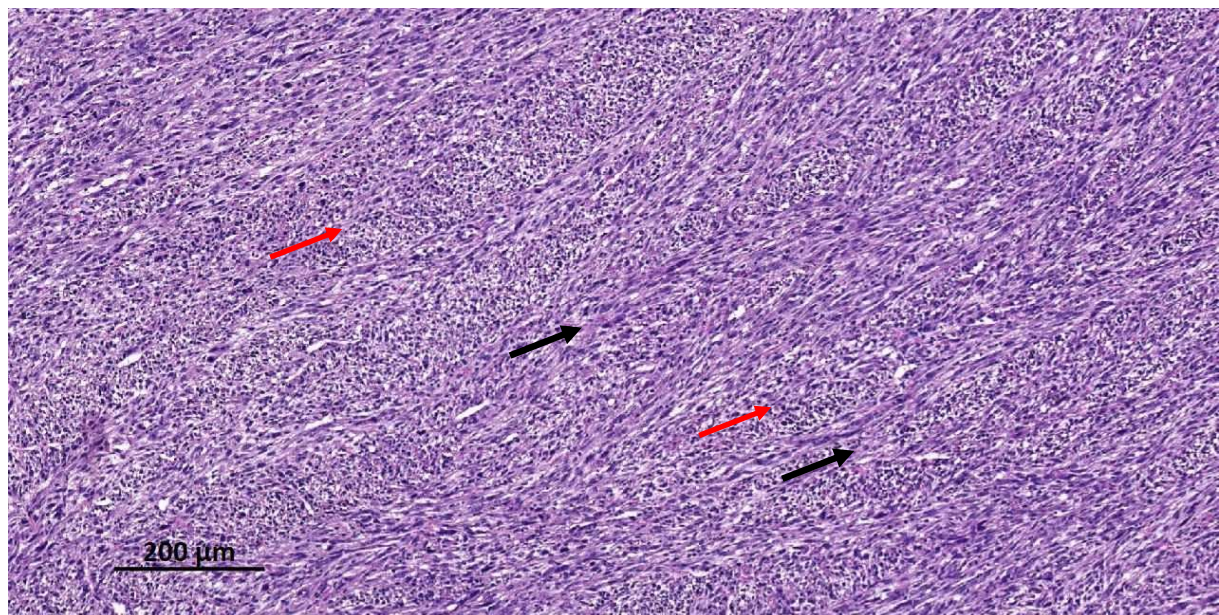


Figure 10: Chemically-induced neoplasms (study #11975): sarcoma, not otherwise specified, male CBA/J mouse 2041/16, MCA s.c.

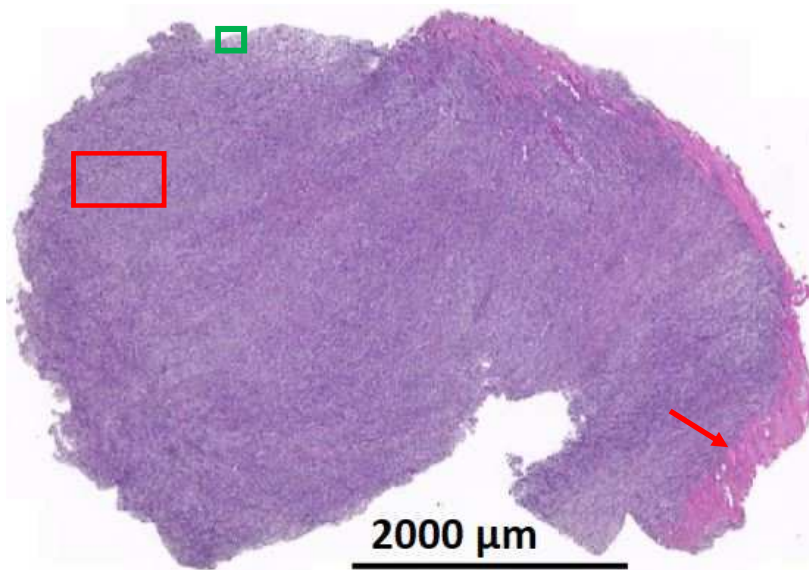


Source: 2017-10-25 13_48_48-TPL811_17_HE_11975_TU_2041_16_4_10_16.czi - ZEN 2.3 lite

Index case: mouse ID number **2041-14**. Strain CBA/J sex: male (♂).

Sarcoma composed of interlacing bundles alternating longitudinal (**black arrows**) and transverse bundles (**black arrows**) or long, rather well differentiated spindle-shaped cells. There is no ischemic necrosis on the section examined.

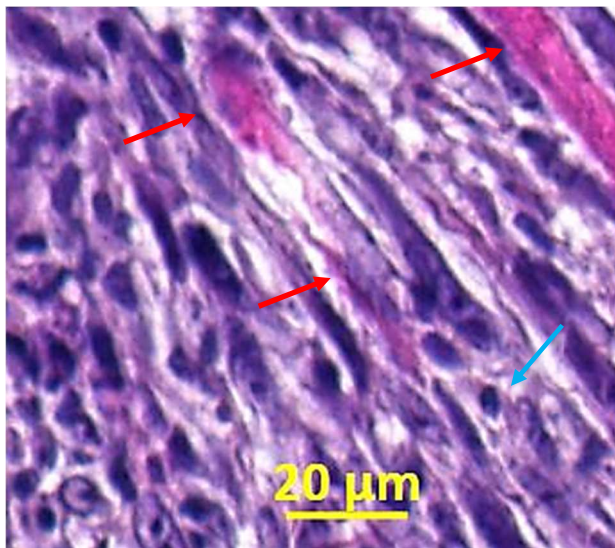
Morphological diagnosis: Sarcoma NOS, MCA-induced, CBA/J mouse.



The **red rectangle** indicates the part of the tumor, which is depicted above.

Notice the homogenous sarcomatous tissue, infiltrating the pre-existing skeletal muscles (**red arrow**) on the edge of the sample.

Source photo file: 2018-01-23 18_36_54-TPL811_17_HE_11975_TU_2041_16_4_10_16.czi - ZEN 2.3 lite

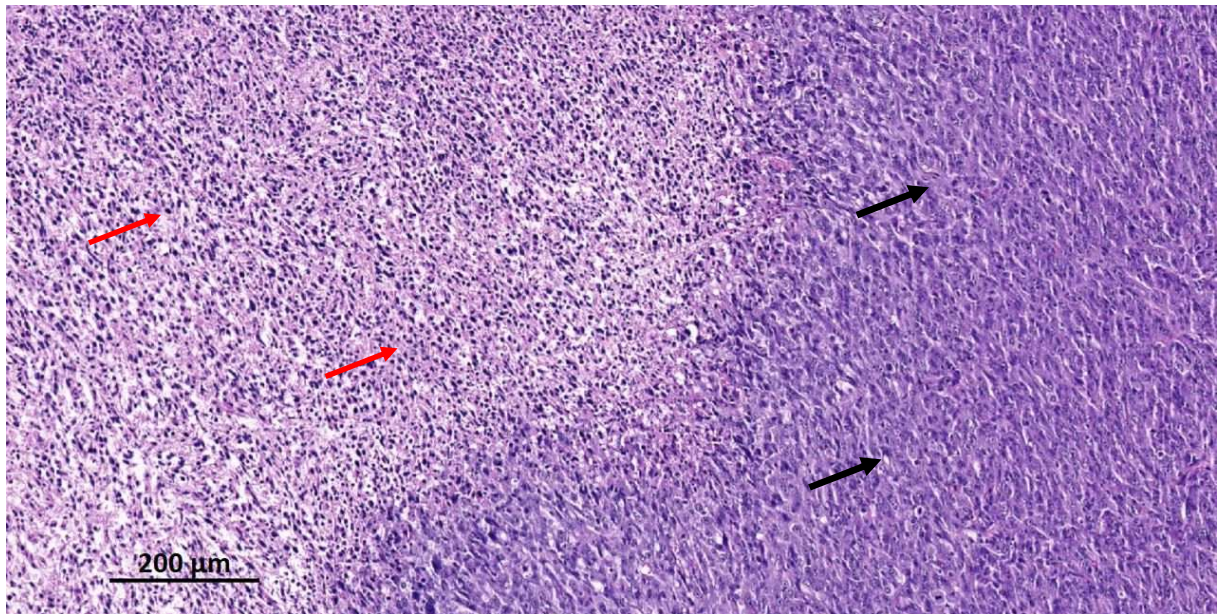


This detail of the neoplastic proliferation is located in the **green rectangle** of the topographical photo above

The neoplastic cells exhibit low pleomorphism but have numerous infiltrating lymphocytes (**blue arrow**) and deeply invade between atrophic muscle fibers (**red arrows**).

Source photo file: 2018-01-23 18_45_19-TPL811_17_HE_11975_TU_2041_16_4_10_16.czi - ZEN 2.3 lite.jpg

Figure 11: Chemically-induced neoplasms (study #11975): sarcoma, not otherwise specified, male CBA/J mouse 1607/16, MCA s.c.

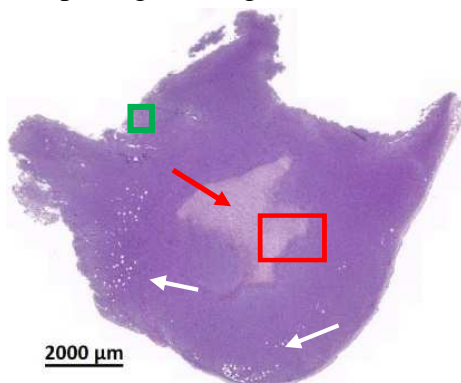


Source: 2017-10-25 13_46_58-TPL811_17_HE_11975_TU_1607_16.czi - ZEN 2.3 lite

Index case: mouse ID number 2041-14. Strain CBA/J sex: male (♂).

The invaded tissue type is unrecognizable (it invades muscle and fat). The sarcoma is composed of poorly intertwined bundles of blastic deeply basophilic roughly spindle-shaped cells (**black arrows**). When compared to the originator neoplasm (see [Figure 10](#)), the main differentiating feature is presence of wide ischemic necrosis indicative of inadequate vascularization (**red arrows**). Lymphocyte infiltration is very dense.

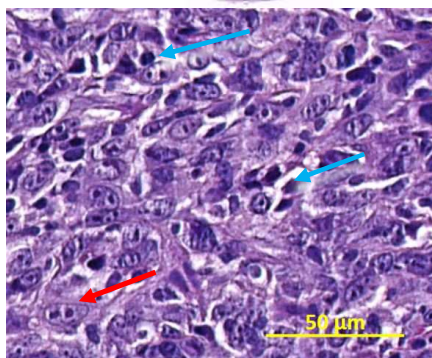
Morphological diagnosis: Sarcoma NOS, MCA-induced, CBA/J mouse.



Source photo file: 2018-01-23 18_15_27-TPL811_17_HE_11975_TU_1607_16.czi - ZEN 2.3 lite

The **red rectangle** indicates the part of the tumor, which is depicted above in [Figure 11](#).

Notice the homogenous sarcomatous deeply basophilic tissue, surrounding the central frankly paler and more eosinophilic area of ischemic necrosis (**red arrow**), and deeply invading/infiltrating the pre-existing fat tissue (white arrows).



Source photo file: 2017-10-25 14_33_05-TPL811_17_HE_11975_TU_1607_16.czi - ZEN 2.3 lite

This detail of the neoplastic proliferation is located in the **green rectangle** of the topographical photo above

Neoplastic cells exhibit relatively low pleomorphism, occasionally prominent nucleoli (**red arrow**) rare mitoses and quite numerous infiltrating small lymphocytes (**blue arrows**). Mitoses are numerous (not shown).

JA-2042 cMDI: NOS sarcoma with hemangiosarcoma-like differentiation

JA-2042/0124-17: NOS sarcoma, with conserved hemangiosarcoma-like (angiod) regions

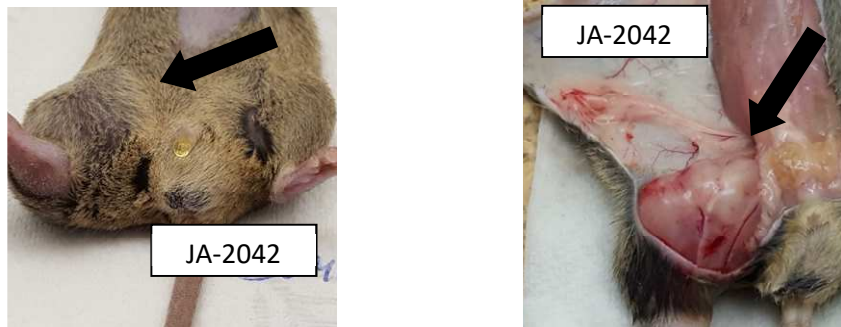
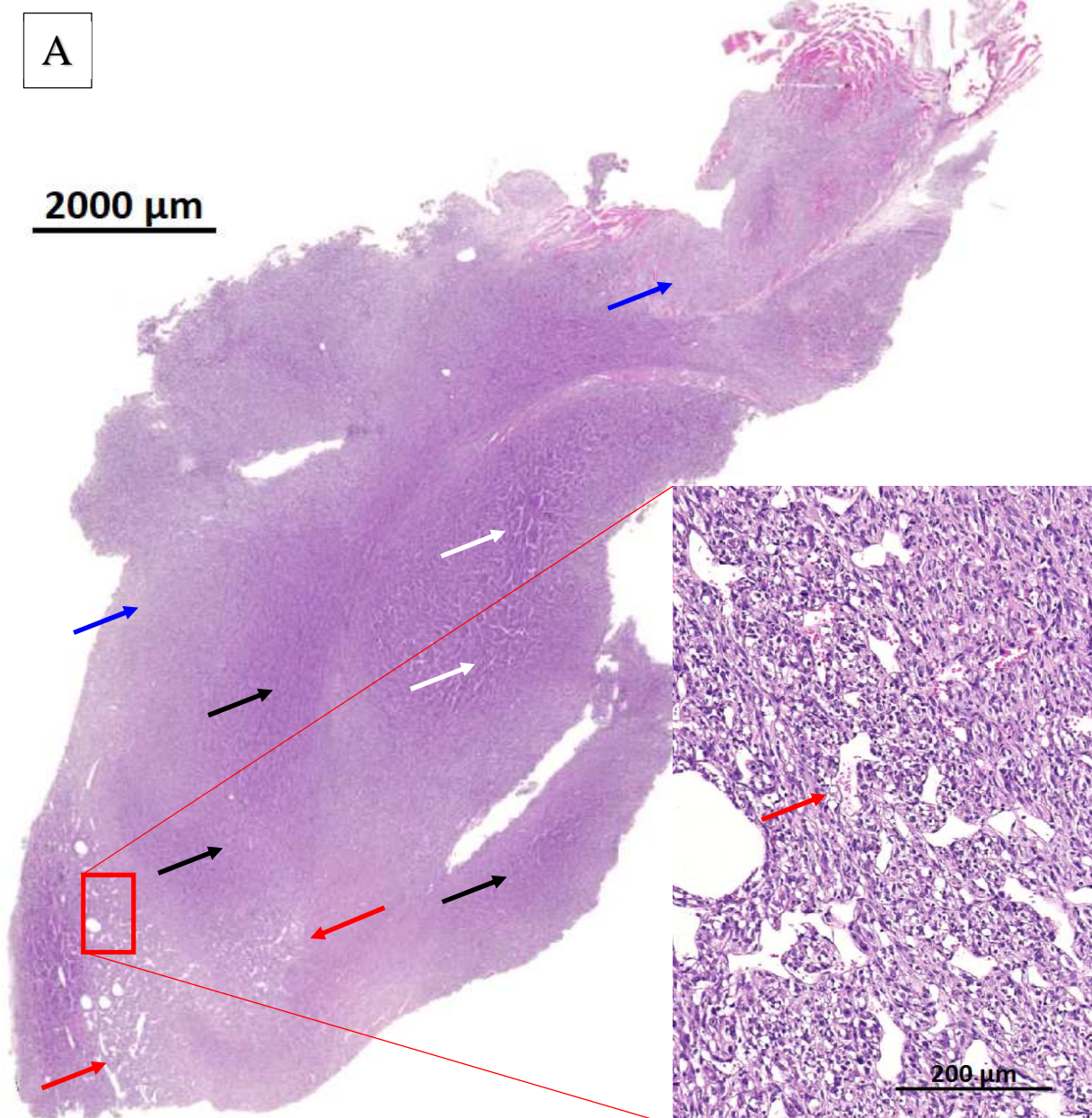
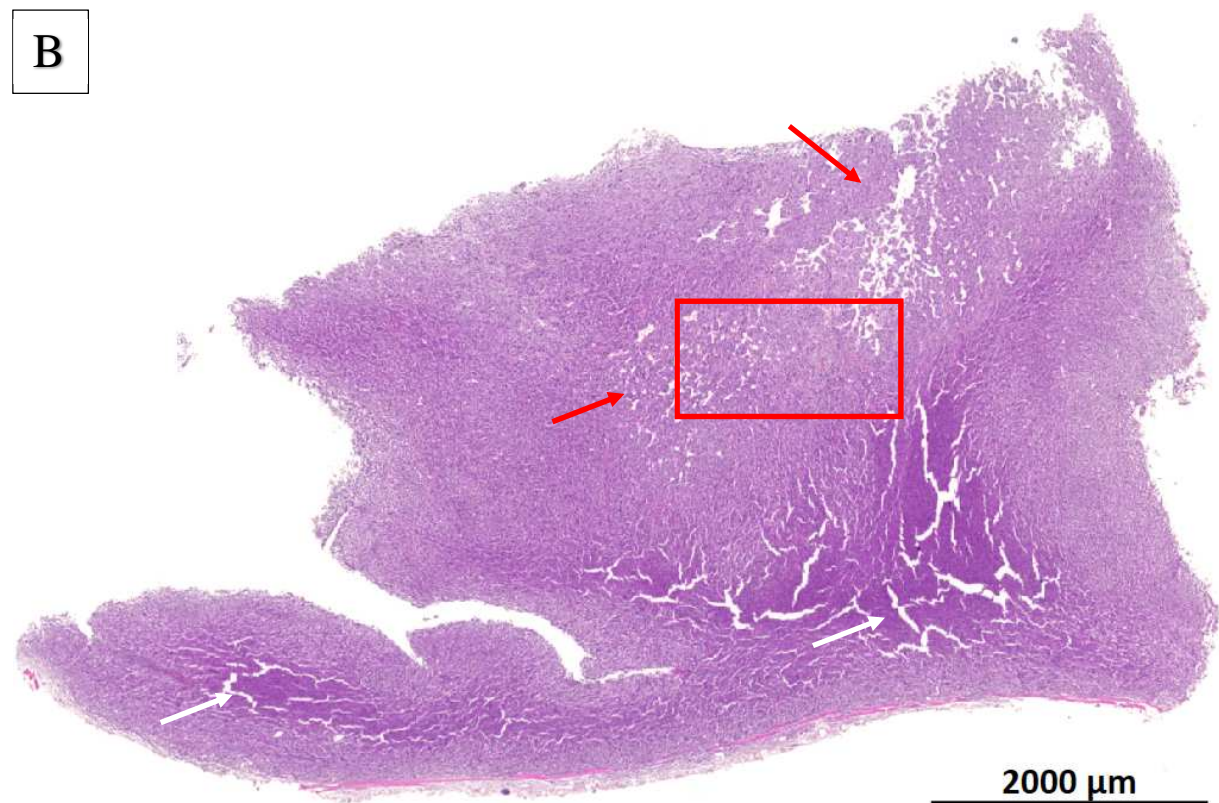


Figure 12: Low magnification (sub-gross aspect) of the tumor masses: **A** index tumor 2042-16 and **B**: established daughter tumor 124-17



A: main mass of the index tumor showing 2 distinct cell density aspects, a higher more basophilic aspect (**black arrows**) and a lower paler and pinker aspect (**blue arrows**) corresponding to lower cell density with also possibly paler cytoplasm. In addition there are 2 small areas with dilated vessels containing red blood cells, mimicking an hemangioma or hemangiosarcoma differentiation (see **red arrows** and **red rectangle** in previous page)

Also, notice artefactual cracks in central areas of the sample (white arrows), suggesting lack of significant extracellular matrix.



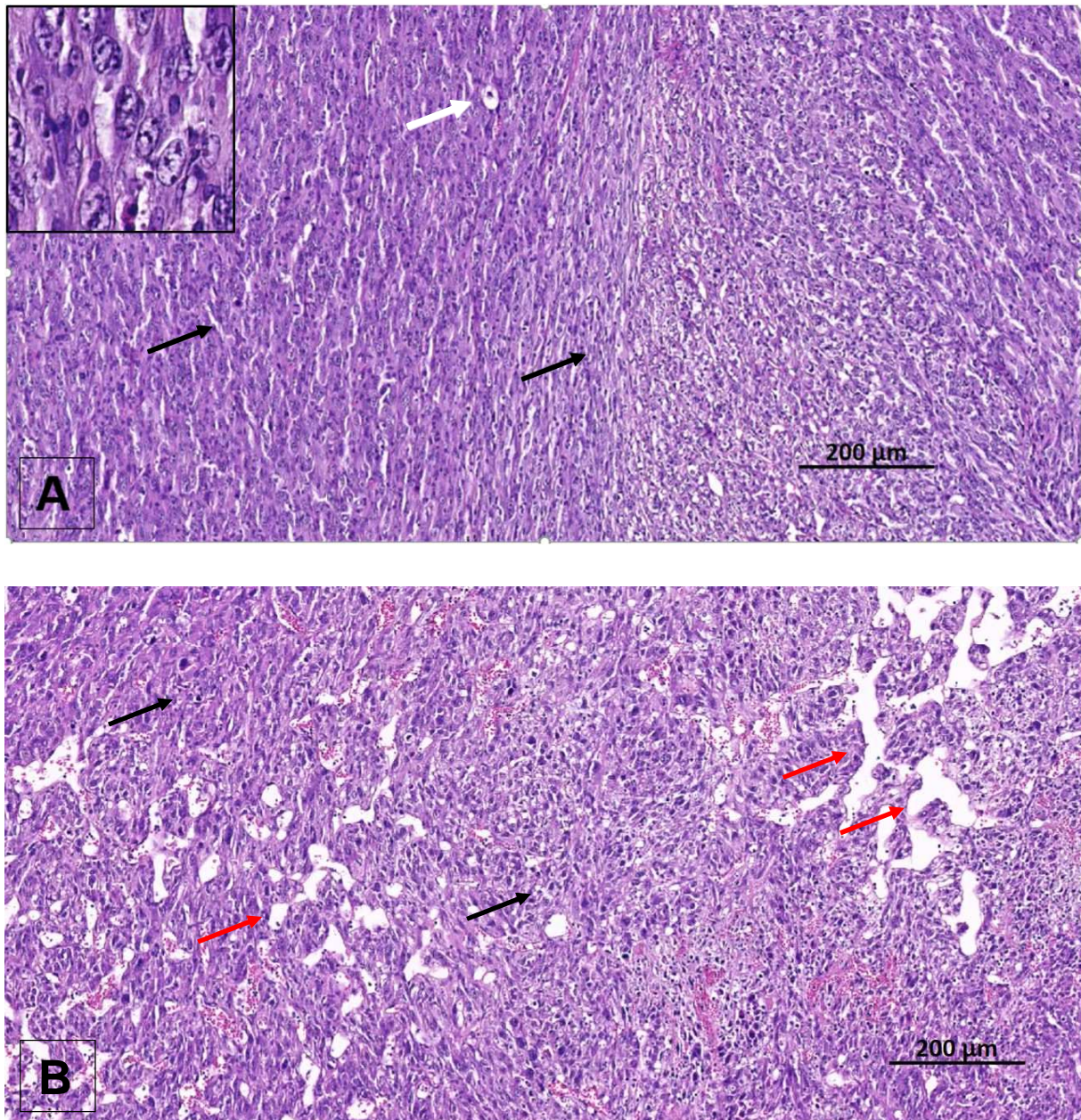
B: Sub-gross view of grafted JA-2042 into **124-17** mouse. The tissue similarity at this magnification is striking. Importantly, there are vascular profiles (see red arrow

There is also hemangiosarcoma differentiation, indicating remarkable phenotype stability (see **red arrows** and **red rectangle**). IHC is strongly advised here to document possible vascular differentiation.

Notice artefactual cracks in central areas of the sample (white arrows), suggesting lack of significant extracellular matrix.

Source file: C:\Users\TLEMARCHAND\Documents\ProQinase-Paper-Project\neue bilds\2019-01-24 15_15_40-#12551 124-17.czi - ZEN 2.3 lite.png; Extracted from TPL Study Phase Number 780/17

Figure 13: Comparison of different regions of index **2042-16** and derived **124-17**



From index case: mouse ID number 2042-16. Strain CBA/J ♀. Induced with MCA.

Sarcoma, not otherwise specified (NOS), composed of interwoven bundles of spindle-shaped elongated cells with plump nuclei (see inset: neoplastic mesenchymal cells), with minimum anaplasia and clearer and denser areas (**black arrows**). Both the index and the established tumor either invades adjacent to blood vessels or exhibit vascular (angio-) differentiation, mimicking an hemangiosarcoma (**B: red arrows**). The index tumor also has rare spaces, related to single cell degeneration (**A: white arrow**). Notice the remarkable phenotypic stability, at least morphologically with H&E stain, when comparing the index (**A**) and derived (**B**) neoplasms. IHC is strongly advised here.

A: Image ID: 2017-10-24 17_39_33-11975_tu__2042-16__2042-16.czi - ZEN 2.3 lite – index case (mouse ID) **2042-16**; **B:** image ID: 2017-10-24 17_36_31-12551_124-17__Establish.czi - ZEN 2.3 lite – ID #**124-17**:

JA-2034 cMDI: NOS sarcoma within adipose tissue of the panniculus

JA-2034/0125-17: NOS sarcoma with adipose tissue of the panniculus

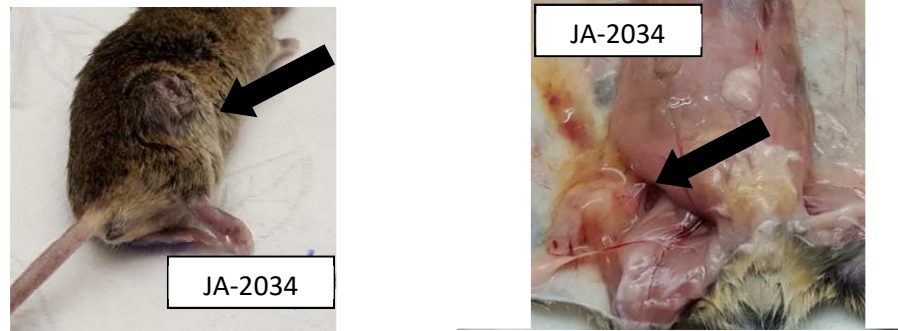
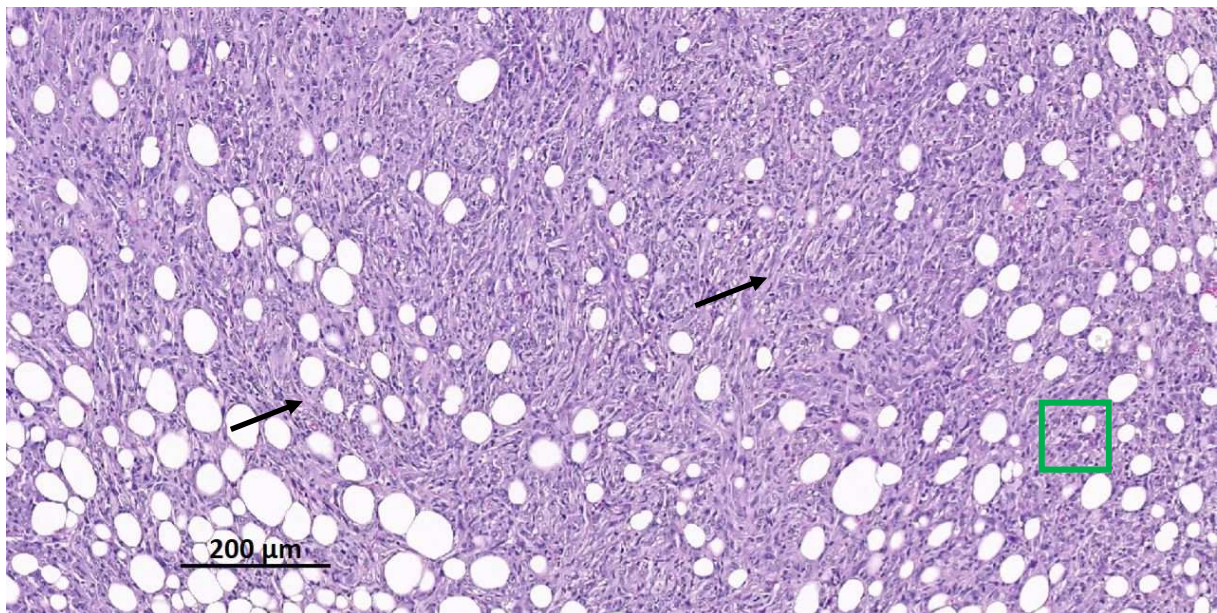


Figure 14: Chemically-induced neoplasms (study #11975): sarcoma, not otherwise specified, male CBA/J mouse 2034/16, MNU s.c.

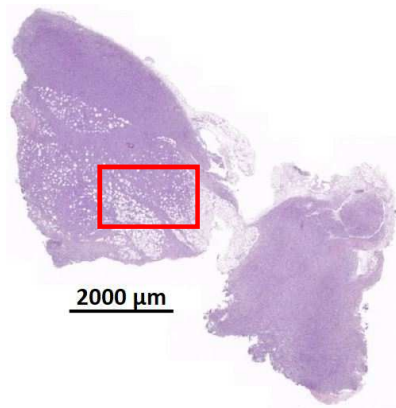


Source: 2017-10-25 13_51_00-TPL811_17_HE_11975_TU_2034_16.czi - ZEN 2.3 lite

Index case: mouse ID number 2034-14. Strain CBA/J sex: male (♂).

The adipose tissue of the panniculus is diffusely invaded by bundles of spindle-shaped cells, rather well differentiated, and of moderate anaplasia (see below; **black arrows**). Based on these samples, it is impossible to state whether the sarcoma NOS simply invades the panniculus or in fact exhibit liposarcomatous differentiation. Based on the normal aspect of the adipocytes, it is most likely that it is a sarcoma invading pre-existing normal adipose tissue?

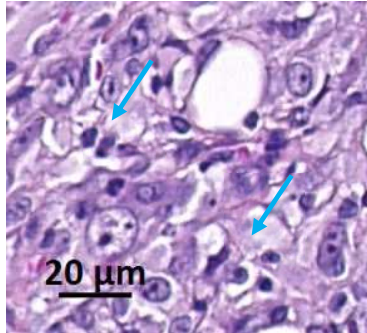
Morphological diagnosis: Sarcoma NOS, MNU-induced, CBA/J mouse.



Source photo file: 2018-01-23 11_08_19-TPL811_17_HE_11975_TU_2034_16.czi - ZEN 2.3 lite

The **red rectangle** indicates the part of the tumor, which is depicted above (top large photo).

The tissue site of invasion is hypodermis (panniculus). Ischemic necrosis is absent

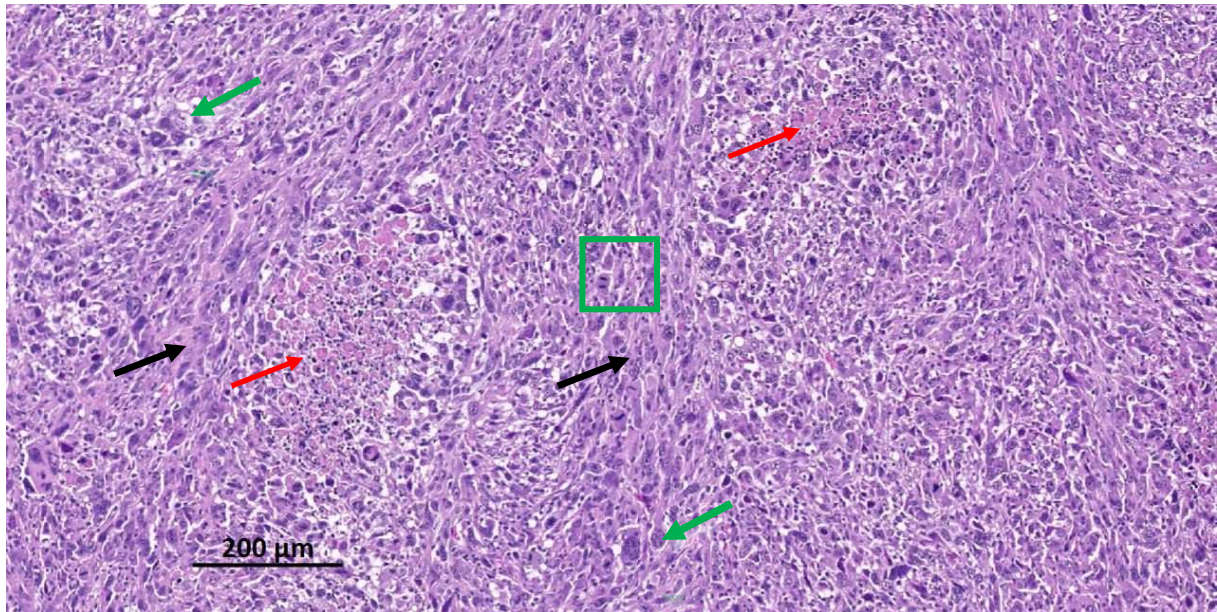


Source photo file: 2018-01-23 11_19_42-TPL811_17_HE_11975_TU_2034_16.czi - ZEN 2.3 lite

This detail of the neoplastic proliferation is located in the **green rectangle** of the top photo above

Neoplastic cells exhibit moderate pleomorphism (no bizarre anaplastic cells) and numerous small infiltrating lymphocytes (**blue arrows**).

Figure 15: Chemically-induced neoplasms (study #11975): sarcoma, not otherwise specified, male CBA/J mouse 0125/17, MNU s.c.

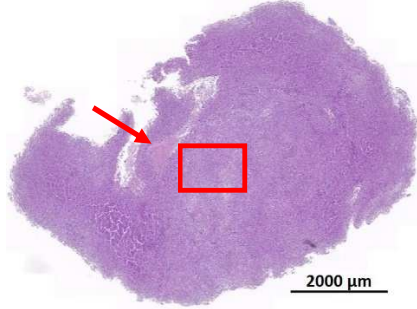


Source: 2017-10-25 13_52_20-TPL811_17_HE_11975_TU_0125_17.czi - ZEN 2.3 lite

Index case: mouse ID number 2034-14. Strain CBA/J sex: male (♂)

The invaded tissue type is unrecognizable. The sarcoma is composed of interlacing bundles of blastic poorly differentiated spindle-shaped cells (**black arrows**). When compared to the originator neoplasm (see [Figure 14](#)), there is an increased degree of anaplasia, more mitoses, with few bizarre giant cells (**green arrows**) and evidence of limited early ischemic necrosis, indicative of inadequate vascularization (**red arrows**).

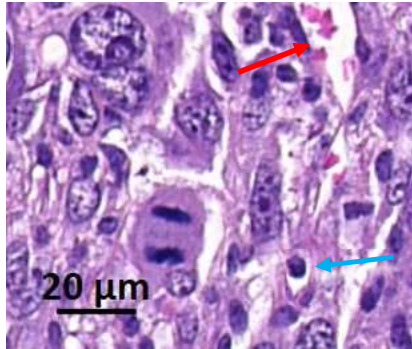
Morphological diagnosis: Sarcoma NOS, MNU-induced, CBA/J mouse, 0125-17.



Source photo file: 2018-01-23 12_13_10-TPL811_17_HE_11975_TU_0125_17.czi - ZEN 2.3 lite

The **red rectangle** indicates the part of the tumor, which is depicted above.

Notice the homogenous sarcomatous tissue, with visible, slightly paler and more eosinophilic ischemic necrosis (**red arrow**).



Source photo file: 2018-01-23 12_11_18-TPL811_17_HE_11975_TU_0125_17.czi - ZEN 2.3 lite

This detail of the neoplastic proliferation is located in the **green rectangle** of the top photo above

Neoplastic cells exhibit significant pleomorphism (with coarser nuclear chromatin and large nucleoli), and numerous mitoses and infiltrating lymphocytes (**blue arrow**). The blood vessel has very thin stroma (**red arrow**)

JA-2043 cMDI: NOS sarcoma with varying aspects from well differentiated to anaplastic

JA-2043/0074-17: NOS sarcoma with varying aspects from well differentiated to moderately
Figure 16: Macroscopic aspects of the tumor JA-2043

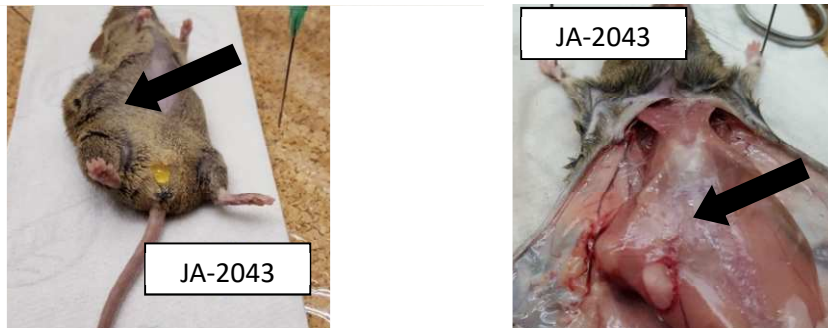
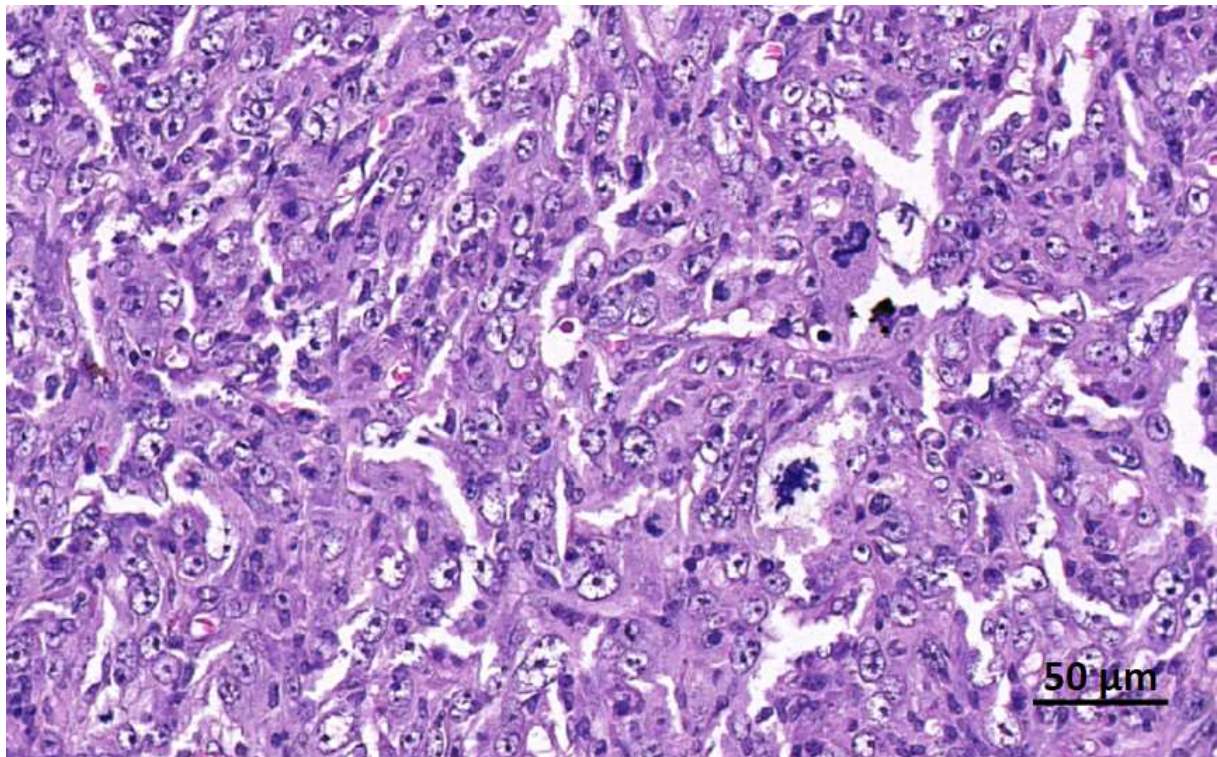


Figure 17: High magnification aspects of the index tumor 2043-16: anaplastic



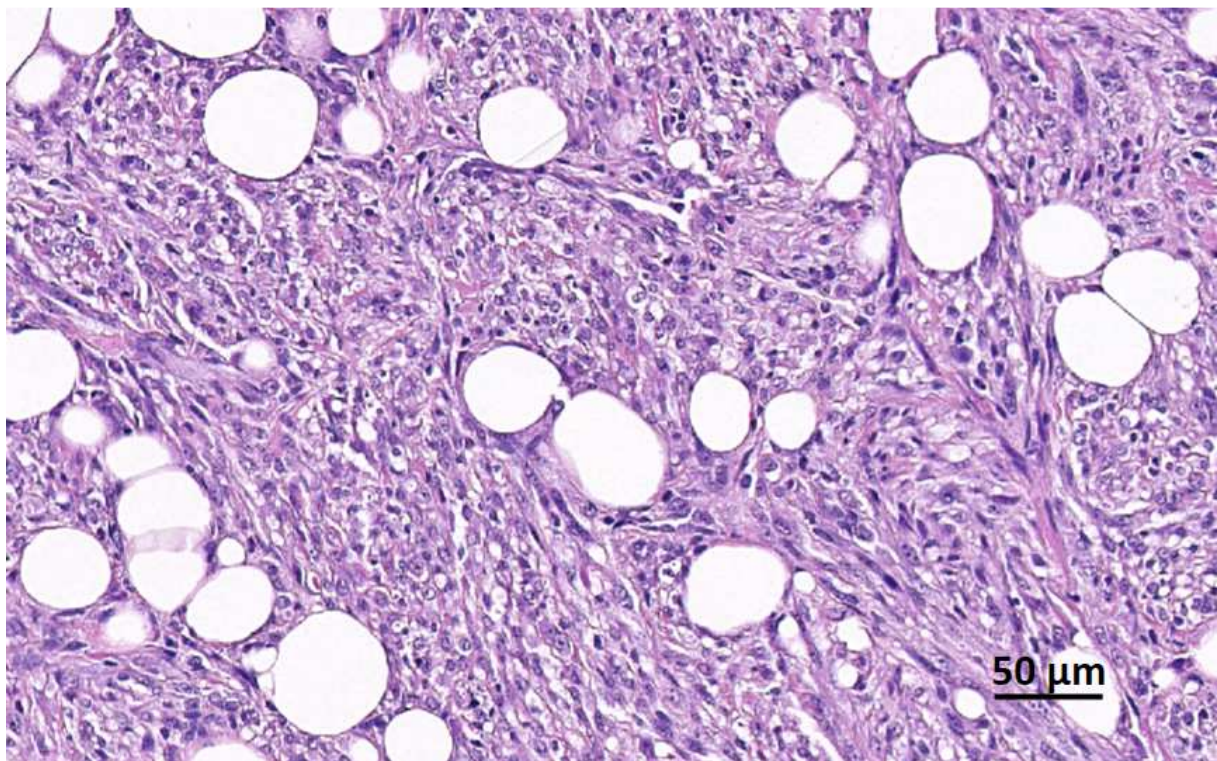
The sarcomatous tissue is characterized by high variability of size and shape of cells and nuclei (“anisopoikilocytosis” and “anisopoikilokaryosis”), vesicular nuclei and multinucleated cells with condensed nuclei and/or abnormal /abortive mitoses or “mitonecrosis” (see **black arrows**) – the section has some artefactual cracks. This is an example of moderate to low differentiation, with a rather anaplastic aspect. This aspect is on the top specimen of [Figure 18](#).

Tumor diagnosis (HE evaluation) - with description	Other comments
Sarcoma NOS, varying aspects, from well differentiated to moderately anaplastic; no giant cells	- deeply invading the skin up to the upper dermis - many anaplastic features (abnormal mitoses, large vesicular nuclei) but no giant multinucleate cells

Figure 18: Low magnification (sub-gross aspect) of the tumor masses of the index tumor 2043-16



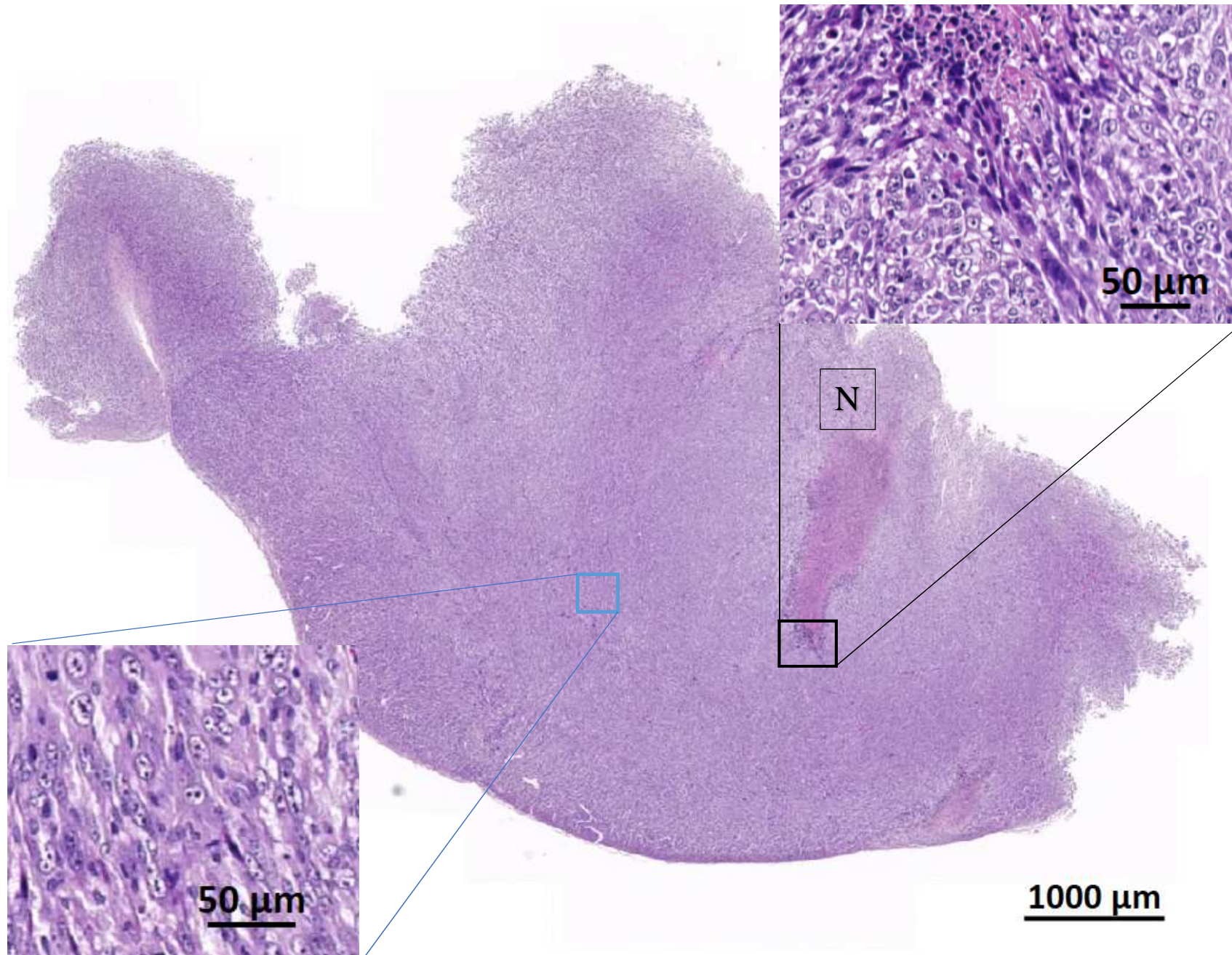
Figure 19: High magnification aspects of the index tumor 2043-16: fusiform aspects



The tumor tissue is characterized by interwoven basket weave bundles of rather well differentiated fibroblasts, which however finely invade and dissect the pre-existing sheets of normal adipocytes of the subcutis.

This aspect is on the low specimen of [Figure 18](#). Extracted from TPL Study Phase Number 811/17

Figure 20: Sub-gross and higher views of grafted JA-2043 into 0074-17 mouse. Tissue similarity with top index tumor at these magnifications is striking. N is central ischemic necrosis of the tumor

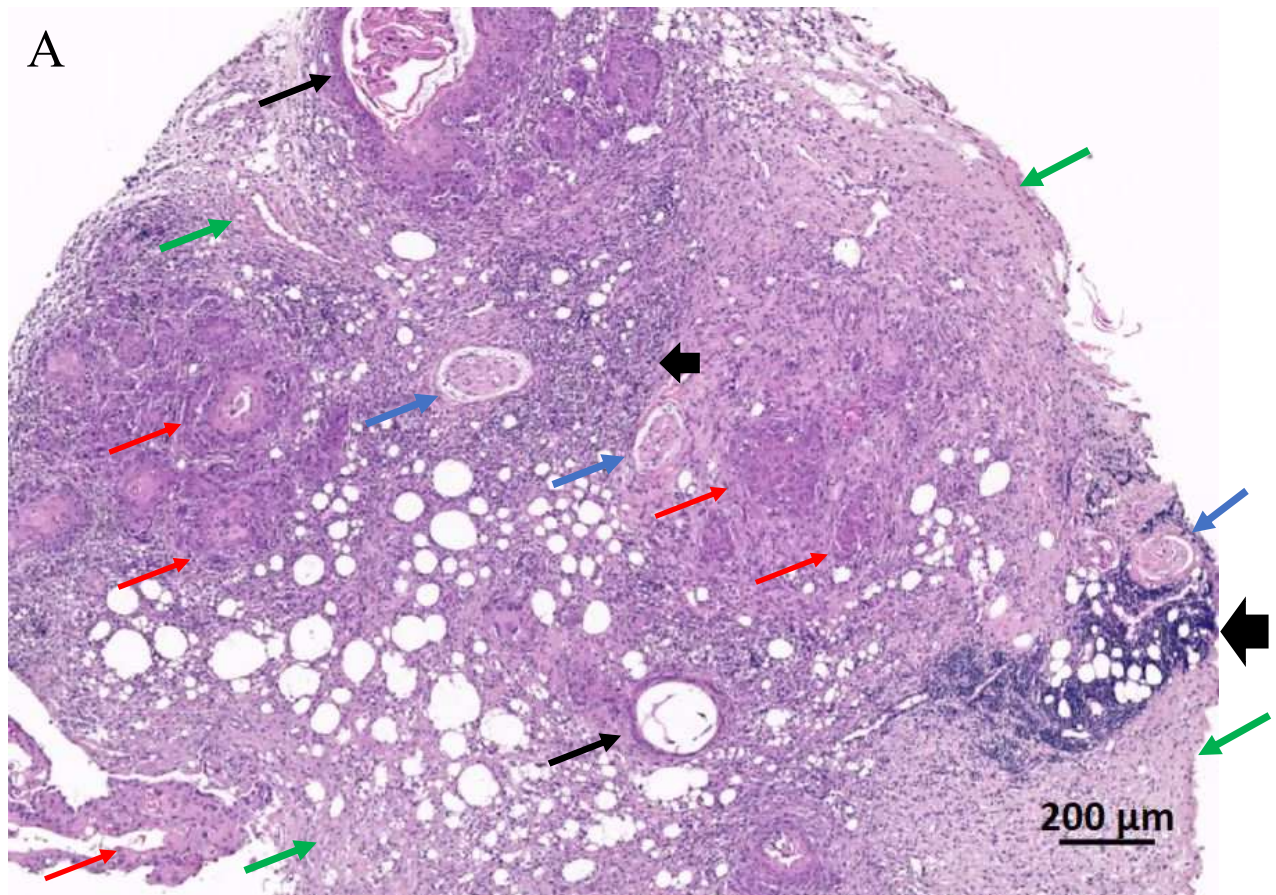


JA-2044 cMDI: Spinocellular carcinoma (epidermoid carcinoma)

JA-2044/1418-16: Spinocellular carcinoma (epidermoid carcinoma) which is an epithelial (epidermal and/or adnexae) neoplastic proliferation


no *in situ* Foto

Figure 21: Chemically-induced neoplasms (study #11975): spinocellular carcinoma, male CBA/J mouse 2044/16, MCA s.c.



Source: 2017-10-25 13_37_55-TPL811_17_HE_11975_TU_2044_16_11_10_16.czi - ZEN 2.3 lite

Index case: mouse ID number 2044-14. Strain CBA/J sex: male (♂)

A: This is an epithelial neoplastic proliferation from the skin, characterized by epidermal differentiation and keratin production, which induces intense inflammation, with a pronounced lymphoid component (**arrowheads** ) , as well as fibrosis (**green arrows**).

It is characterized by cords and nodular elements of keratinocytes (**red arrows**) with central laminar keratinization, often forming central cysts with occasional horn pearls (**black arrow**). The neoplasm is entrapping a nerve (**blue arrows**).

Morphological diagnosis: Spinocellular carcinoma, skin, MCA-induced, CBA/J mouse.

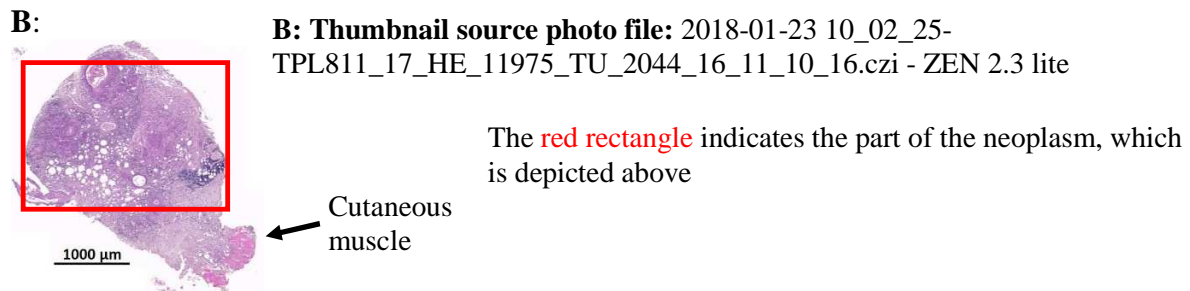
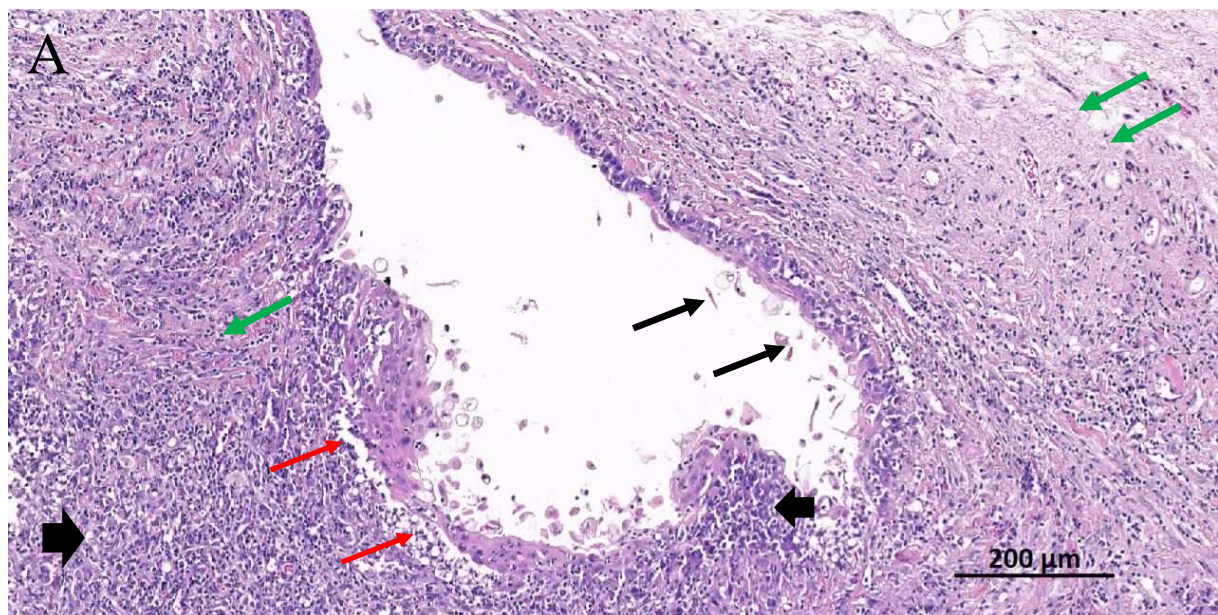


Figure 22: Chemically-induced neoplasms (study #11975): spinocellular carcinoma, male CBA/J mouse 1418/16, MCA s.c.



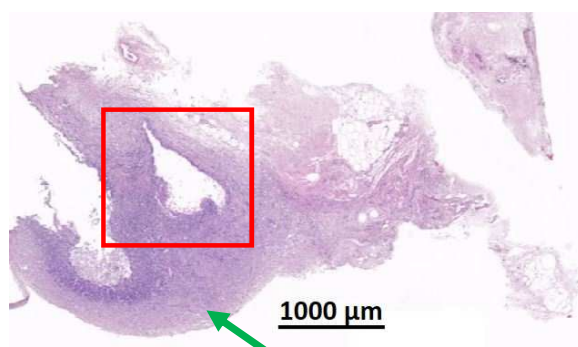
Source: 2017-10-25 13_43_16-TPL811_17_HE_11975_TU_1418_16.czi - ZEN 2.3 lite

Index case: mouse ID number 2044-14. Strain CBA/J sex: male (♂)

A: The epithelial proliferative component of this tumor is again the neoplastic epidermal spinocellular (keratocytic) elements (**red arrows**) mostly forming cystic spaces, in which the dyskeratotic keratinization occurs without horn pearl formations (**black arrows**). However, the majority of the tumor (see below panel B) is composed of florid (desmoplastic) fibrosis (**green arrows**) and intense lymphocytic infiltrative () stromal elements, underlining the similarity with the neoplasm depicted in [Figure 21](#).

Morphological diagnosis: Spinocellular carcinoma, skin, MCA-induced, CBA/J mouse

B: Low magnification of tumor aspect overview (thumbnail):



The **red rectangle** indicates the part of the neoplasm, which is depicted above

The vast majority of the tumor on the section examined is composed of desmoplastic and highly inflamed stroma (**green arrow**).

Source photo file: 2018-01-23 10_17_10-TPL811_17_HE_11975_TU_1418_16.czi - ZEN 2.3 lite

Note: ID = identification code

Animal	Spec. ID (loc)	originator	Tumor diagnosis (HE evaluation)	Comments
2044-16	#11975_1 2044/16 11.10.16	2044-14	spinocellular carcinoma	intense lymphoid and neutrophilic inflammation
1418-16	#11975_Tu 1418/16	2044-14	spinocellular carcinoma	high levels of inflammation; glandular differentiation

JA-2017 cMDI: NOS sarcoma varying from well differentiated to moderately anaplastic; no giant cells

JA-2017/1573-16: NOS sarcoma varying from well differentiated to moderately anaplastic; no giant cells.

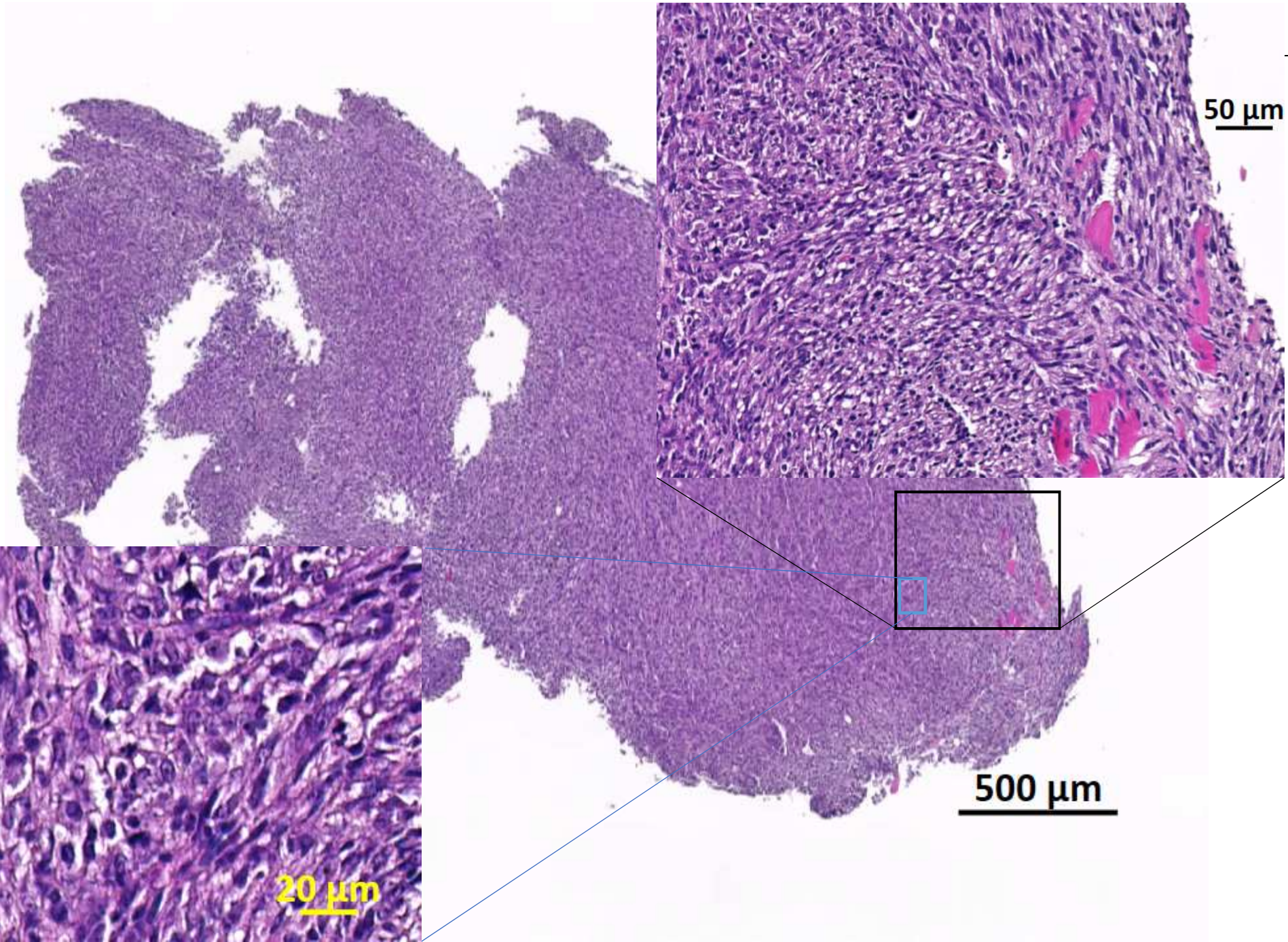
The re-transplanted tumors grow only in SCID/bg



Animal	Spec. ID (loc)	originator	Tumor diagnosis (HE evaluation) - with comments	Comments for next step(s)
2017-16	#11975_Tu 2017/16	2017-14	Sarcoma NOS, varying aspects, from well differentiated to moderately anaplastic; no giant cells	Na – see Figure 24
1573/16	#11975_Tu 1573/16	2017-14	Sarcoma NOS, varying aspects, from well differentiated to moderately anaplastic; no giant cells	abundant ischemic necrosis – see Figure 25 and Figure 26

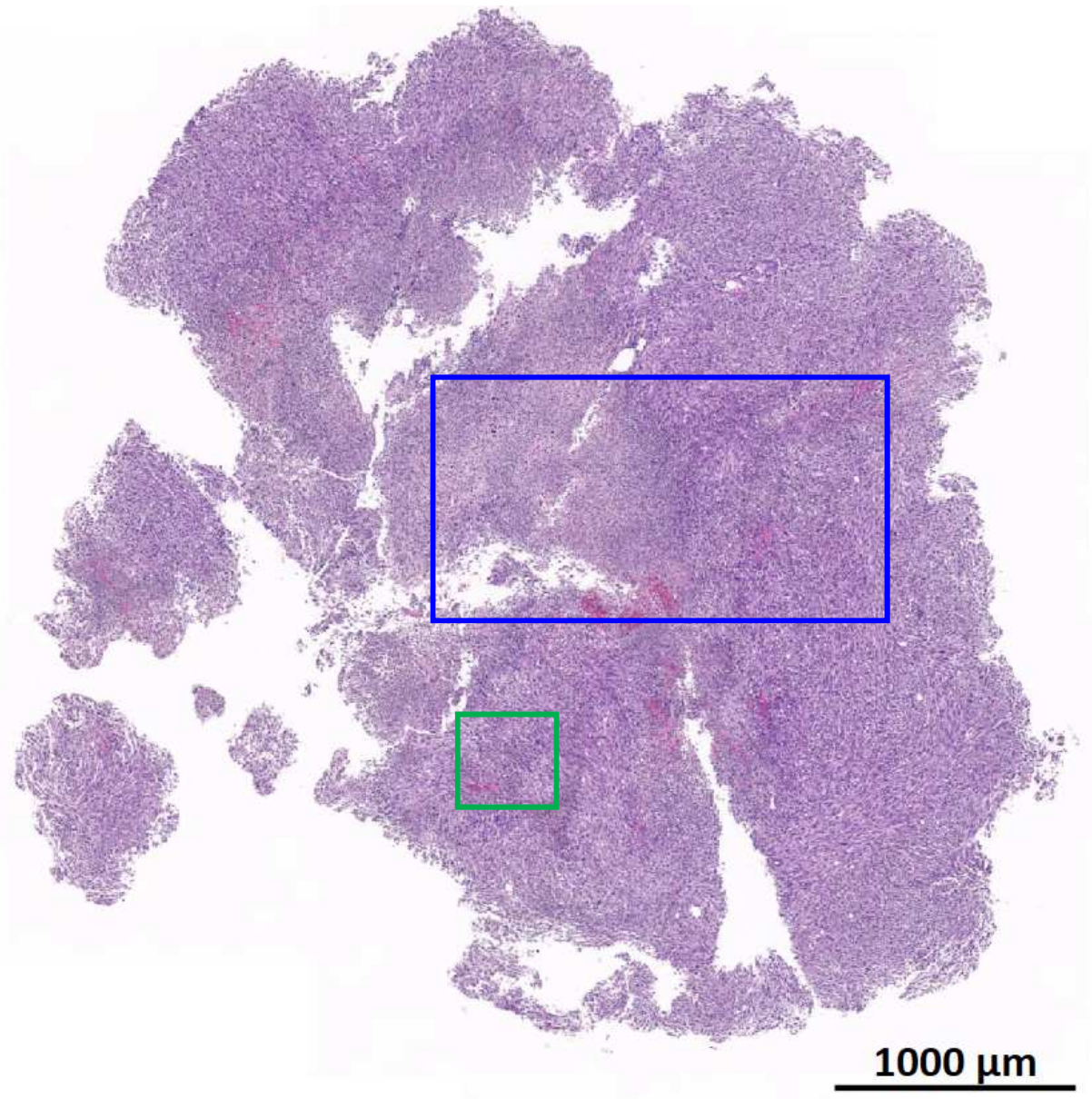
Figure 23: Originator tumor of the JA-2017: **2017-16** (see next page)

There is presence of bundles of relatively homogenous blastic spindle-shaped cells (lower left inset), which destroy and dissect the pre-existing skeletal striated muscles (upper right inset)
Please see next page (landscape)
(see next page)





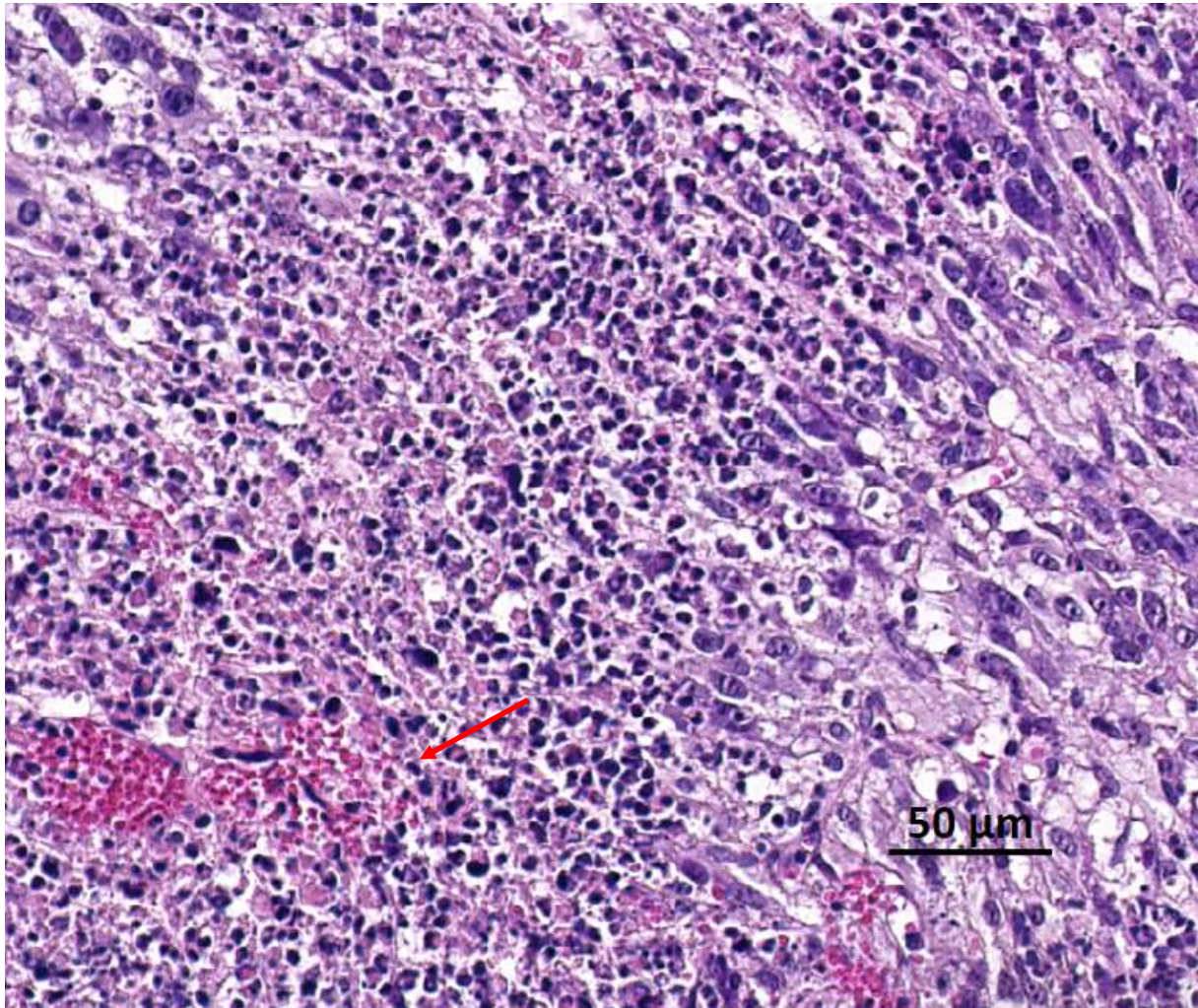
1 **Figure 24:** Low magnification aspect of the derived **tumor 1573-16** grafted with **JA-**
2 **2017**



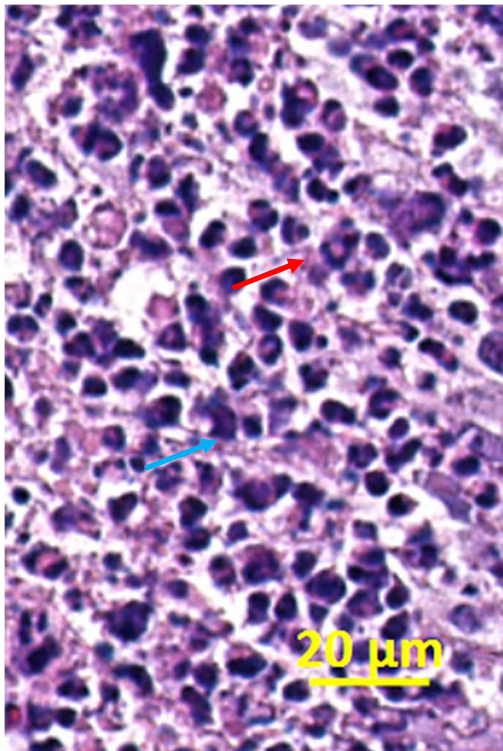
3
4
5
6
7
8
9
10
11
12

The tumor is fragmented and has several areas of necrosis of tumor tissue separated by a relatively dense line of intact and degenerating inflammatory cells, encompassing neutrophils and mononuclear cells, including relatively numerous small lymphocytes

13 **Figure 25:** Tumor 1573-16: High magnification view of the region in the **Green**
14 **square**



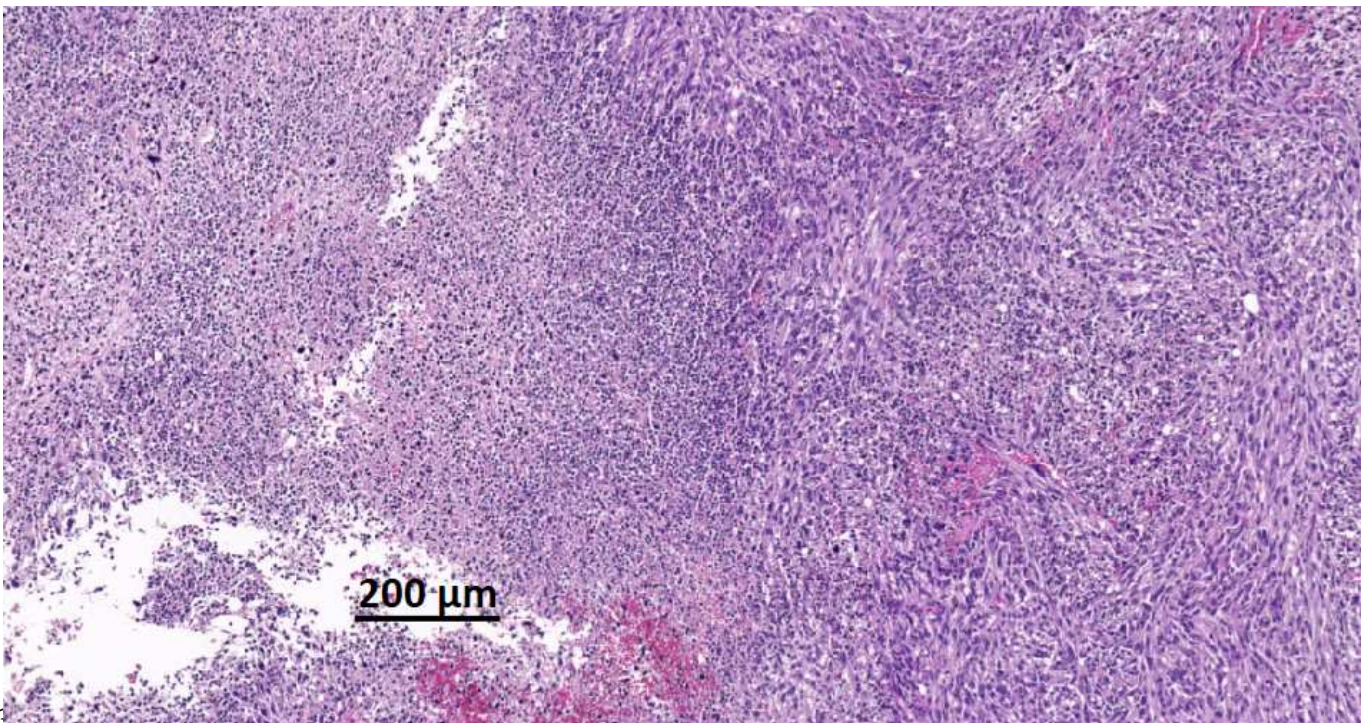
15
16 The inflammatory cells composing the interface of intact and degenerated neoplastic tissue
17 (with hemorrhage) is mainly composed of intact and degenerated granulocytes, with focal
18 presence of mononuclear cells (see inset below next page). In central ischemic necrosis there
19 is associated red blood cell extravasation (**red arrows**).



Detail of the [Figure 25](#) depicting the cytological details of the inflammatory infiltration at the interface of the intact and degenerated neoplastic tissue, with mainly intact and degenerated granulocytes ([red arrow](#)). Mononuclear cells suggesting monocytes and/or lymphocytes are relatively rare ([blue arrow](#))

20

21 [Figure 26](#) : Tumor 1573-16: Medium magnification view of the region in the large
22 [blue rectangle](#) from figure 24



23

24

25 Areas of necrosis are numerous and coalescing with hemorrhage and abundant leukocytes:

26 Extracted from TPL Study Phase Number 811/17

27 **Abbreviation list**

28

AdK = ADC	Adenocarcinoma
DDX. = Diff. Dx.	Differential diagnosis
BALT	Bronchus associated lymphoid tissue
Bein	Leg
Brustdrüse = rü	Mammary gland
Darm	Intestinal
H&E = HE	Hematoxylin and eosin
ID	Identification
IHC	Immunohistochemistry
K	Carcinoma
Leb	Liver (Leber)
MCA	Methylcholanthrene
MNU	1-methyl-1-nitrosourea
MGCs	Multinucleate giant cells (syncytial macrophages or neoplastic cells)
mz	Spleen (Milz)
NA	Not applicable
Niere = ni = nie	Kidney
NOS	Not otherwise specified
PND	Post-natal Day
S	Sarcoma
s.c.	Sub-cutaneous
SCID	Severe Combined Immuno-Deficiency
Spec.	Specimen
TIL	Tumor infiltrating lymphocytes

29

30



© 2018 by the authors. Submitted for possible open access publication under the terms and conditions of the Creative Commons Attribution (CC BY) license

33 (<http://creativecommons.org/licenses/by/4.0/>).